

A Gaussian mixture model representation of endmember variability in hyperspectral unmixing

Yuan Zhou, Anand Rangarajan and Paul Gader
 Dept. of Computer and Information Science and Engineering
 University of Florida, Gainesville, FL, USA
 E-mail: {yuan,anand,pgader}@cise.ufl.edu

March 1, 2022

Abstract

Hyperspectral unmixing while considering endmember variability is usually performed by the normal compositional model (NCM), where the endmembers for each pixel are assumed to be sampled from unimodal Gaussian distributions. However, in real applications, the distribution of a material is often not Gaussian. In this paper, we use Gaussian mixture models (GMM) to represent the endmember variability. We show, given the GMM starting premise, that the distribution of the mixed pixel (under the linear mixing model) is also a GMM (and this is shown from two perspectives). The first perspective originates from the random variable transformation and gives a conditional density function of the pixels given the abundances and GMM parameters. With proper smoothness and sparsity prior constraints on the abundances, the conditional density function leads to a standard maximum *a posteriori* (MAP) problem which can be solved using generalized expectation maximization. The second perspective originates from marginalizing over the endmembers in the GMM, which provides us with a foundation to solve for the endmembers at each pixel. Hence, our model can not only estimate the abundances and distribution parameters, but also the distinct endmember set for each pixel. We tested the proposed GMM on several synthetic and real datasets, and showed its potential by comparing it to current popular methods.

1 Introduction

The formation of hyperspectral images can be simplified by the *linear mixing model* (LMM), which assumes that the physical region corresponding to a pixel contains several pure materials, so that each material contributes a fraction of its spectra based on area to the final spectra of the pixel. Hence, the observed spectra $\mathbf{y}_n \in \mathbb{R}^B$, $n = 1, \dots, N$ (B is the number of wavelengths and N is the number of pixels) is a (non-negative) linear combination of the pure material (called *endmember*) spectra $\mathbf{m}_j \in \mathbb{R}^B$, $j = 1, \dots, M$ (M is the number of endmembers), i.e.

$$\mathbf{y}_n = \sum_{j=1}^M \mathbf{m}_j \alpha_{nj} + \mathbf{n}_n, \text{ s.t. } \alpha_{nj} \geq 0, \sum_{j=1}^M \alpha_{nj} = 1, \quad (1)$$

where $\mathbf{n}_n \in \mathbb{R}^B$ is additive noise. Here, the endmember set $\{\mathbf{m}_j : j = 1, \dots, M\}$ is fixed for all the pixels. This model simplifies the unmixing problem to a matrix factorization one, leading to efficient computation and simple algorithms such as iterative constrained endmembers (ICE), vertex

component analysis (VCA), piecewise convex multiple-model endmember detection (PCOMMEND) [1, 2, 3] etc., which receive comprehensive reviews in [4, 5].

However, in practice the LMM may not be valid in many real scenarios. Even for a *pure* pixel that only contains one material, its spectra may not be consistent over the whole image. This is due to several factors such as atmospheric condition, topography and intrinsic variability. For example, for vegetation, the canopies will introduce multiple scattering and thus generate different reflectances even from the same trees; for urban scenes, the incidence and emergence angles could be different for the same roof, causing different reflectances; for minerals, the spectroscopy model developed by Hapke also considers the porosity and roughness of the material as variable [6]. To take these factors into consideration, researchers generalized Eq. (1) to a more abstract form $\mathbf{y}_n = F(\{\mathbf{m}_j, \alpha_{nj} : j = 1, \dots, M\})$ and devised specific *nonlinear mixing models* for each scenario. For example, bilinear models were proposed to handle the vegetation case [7], the Hapke model was used to handle minerals [8], and kernels were proposed for flexible nonlinear mixing [9, 10]. A panoply of nonlinear models can be found in the review article [11]. We note that in these models, a fixed endmember set is still assumed while using a more complicated model.

While nonlinear models abound lately, the LMM still has physical significance. To account for real scenarios, researchers have taken another route by generalizing Eq. (1) to

$$\mathbf{y}_n = \sum_{j=1}^M \mathbf{m}_{nj} \alpha_{nj} + \mathbf{n}_n, \quad (2)$$

where $\{\mathbf{m}_{nj} \in \mathbb{R}^B : j = 1, \dots, M\}$, $n = 1, \dots, N$ could be different for each n , i.e. the endmember spectra for each pixel could be different. This is called *endmember variability*, and has also received a lot of attention in the community [12, 13]. Note that given $\{\mathbf{y}_n\}$, inferring $\{\mathbf{m}_{nj}, \alpha_{nj}\}$ is a much more difficult problem than inferring $\{\mathbf{m}_j, \alpha_{nj}\}$ in Eq. (1). Hence, in many papers $\{\mathbf{m}_{nj}\}$ are assumed to be from a spectral library, which is usually called supervised unmixing [14, 15, 16]. On the other hand, if the endmember spectra are to be extracted from the image, we call them unsupervised unmixing models [17, 18, 19, 20, 21, 22].

We can also categorize the papers on endmember variability by how this variability is modeled. In the review paper [13], it can be modeled as a endmember set [22, 16] or as a distribution [17, 18, 14, 15, 19, 20, 21]. Although early works like multiple endmember spectral mixture analysis (MESMA) and endmember bundles tend to use the nonparametric representation [22, 16], they suffer from uncontrollable complexity with increasing spectral library size hence require a laborious library reduction approach [23]. The distribution based approaches assume that the endmembers for each pixel are sampled from probability distributions (e.g. Gaussian, a.k.a. *normal compositional model* (NCM)), hence embrace large libraries and numerically tractable [14]. Here, we give an overview of NCM because of its simplicity and popularity [19, 20, 17, 21, 15, 18].

Suppose the j th endmember at the n th pixel follows a Gaussian distribution $p(\mathbf{m}_{nj}) = \mathcal{N}(\mathbf{m}_{nj} | \boldsymbol{\mu}_j, \boldsymbol{\Sigma}_j)$ where $\boldsymbol{\mu}_j \in \mathbb{R}^B$ and $\boldsymbol{\Sigma}_j \in \mathbb{R}^{B \times B}$, and the additive noise also follows a Gaussian distribution $p(\mathbf{n}_n) = \mathcal{N}(\mathbf{n}_n | \mathbf{0}, \mathbf{D})$ where \mathbf{D} is the noise covariance matrix. The random variable transformation (r.v.t.) (2) suggests that the probability density function of \mathbf{y}_n can be derived as

$$p(\mathbf{y}_n | \boldsymbol{\alpha}_n, \boldsymbol{\Theta}, \mathbf{D}) = \mathcal{N}\left(\mathbf{y}_n \mid \sum_{j=1}^M \alpha_{nj} \boldsymbol{\mu}_j, \sum_{j=1}^M \alpha_{nj}^2 \boldsymbol{\Sigma}_j + \mathbf{D}\right), \quad (3)$$

where $\boldsymbol{\alpha}_n := [\alpha_{n1}, \dots, \alpha_{nM}]^T$, $\boldsymbol{\Theta} := \{\boldsymbol{\mu}_j, \boldsymbol{\Sigma}_j : j = 1, \dots, M\}$. The conditional density function in (3) is usually embedded in a Bayesian framework such that we can incorporate priors and also

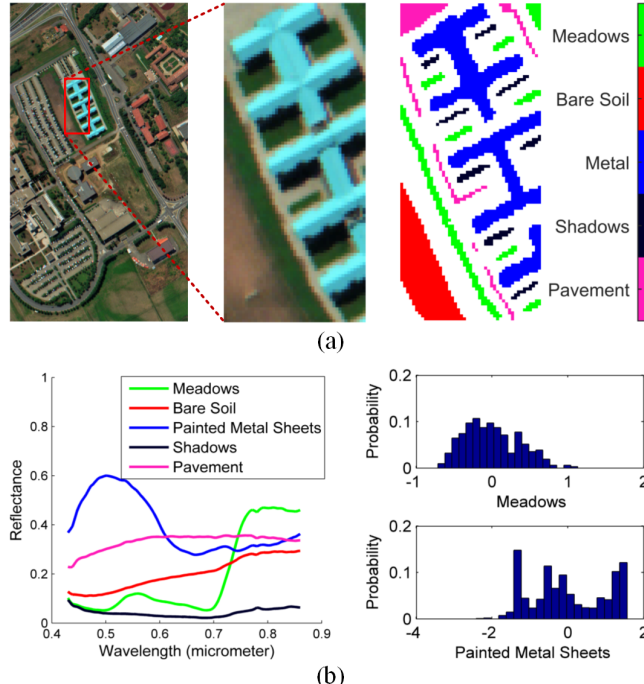


Figure 1: (a) Original Pavia University image and selected ROI with its ground truth image. (b) Mean spectra of the identified 5 endmembers and histograms of meadows and painted metal sheets. PCA is used to project the multidimensional pixels to single values which are counted in the histograms. Although the histogram of meadows may appear to be a Gaussian distribution, that of painted metal sheets is obviously neither a unimodal Gaussian or Beta distribution.

estimate hyperparameters. Then, NCM uses different optimization approaches, e.g. expectation maximization[21], sampling methods[19, 20, 17], particle swarm optimization[18], to determine the parameters $\{\boldsymbol{\mu}_j, \boldsymbol{\Sigma}_j\}$ and $\{\alpha_{nj}\}$.

There are few papers that use other distributions. In [14], Xiaoxiao Du *et al.* note that the Gaussian distribution may allow negative values which are not realistic. In addition, the real distribution may be skewed. Hence, they introduce a Beta compositional model (BCM) to model the variability. The problem is that the true distribution may not be well approximated by any unimodal distribution. Consider the Pavia University dataset shown in Fig. 1, where the multidimensional pixels are projected to one dimension to afford better visualization. Among the manually identified materials, we can see that although the histogram of meadows may look like a Gaussian distribution, that of painted metal sheets has multiple peaks and cannot be approximated by either a Gaussian or Beta distribution. This is due to different angles of these sheets on the roof. Since each piece of metal sheet is tilted, it forms a cluster of reflectances which contributes to a peak in the histogram. This example shows that we should use a more flexible distribution to represent the endmember variability.

In this paper, we use a mixture of Gaussians to approximate any distribution that an endmember may exhibit, and solve the LMM by considering endmember variability. In a nutshell, the Gaussian mixture model (GMM) models $p(\mathbf{m}_{nj})$ by a mixture of Gaussians, say $p(\mathbf{m}_{nj}) = \sum_k \pi_{jk} \mathcal{N}(\mathbf{m}_{nj} | \boldsymbol{\mu}_{jk}, \boldsymbol{\Sigma}_{jk})$, and then obtains the distribution of \mathbf{y}_n by the r.v.t. (2), which turns out to be another mixture of Gaussians and can be used for inferring the unknown parameters. Here, we briefly explain how GMM works intuitively by comparing it to the NCM with the details

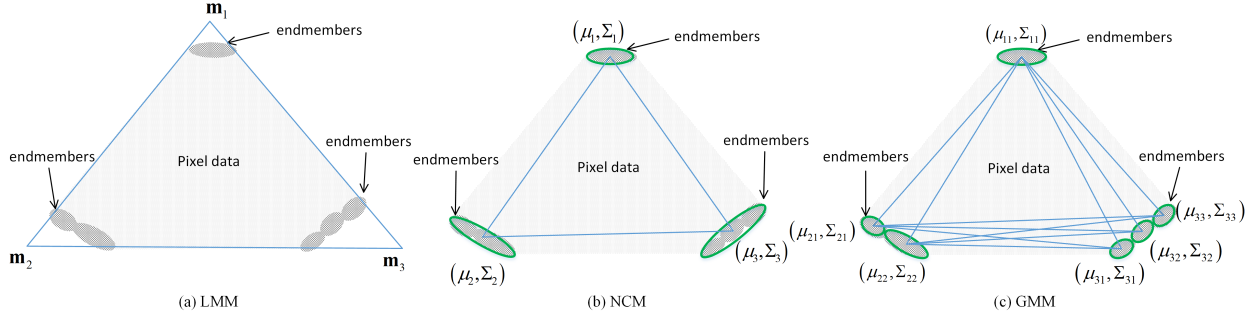


Figure 2: Comparison of the mechanisms among LMM, NCM and GMM. We have 3 endmembers represented by the darken gray areas. LMM tries to find a set of endmembers that fit the pixel data. NCM tries to find a set of Gaussian centers that fit the pixel data, with error weighted by the covariance matrices. GMM tries to find Gaussian centers such that all their linear combinations fit the pixel data, with each weighted by the prior π_k . We may use 6 endmembers with NCM, but then the prior information is lost.

given later. The maximum likelihood estimation (MLE) of NCM (using (3)) aims to find $\{\boldsymbol{\mu}_j\}$ such that its linear combination matches \mathbf{y}_n . Contrary to NCM, GMM aims to find $\{\boldsymbol{\mu}_{jk}\}$ such that *all* its linear combinations match \mathbf{y}_n . Say we have $\boldsymbol{\mu}_{11}, \boldsymbol{\mu}_{21}, \boldsymbol{\mu}_{22}, \boldsymbol{\mu}_{31}, \boldsymbol{\mu}_{32}, \boldsymbol{\mu}_{33}$: then there are 6 combinations as explained in Fig. 2, but with emphasis weighted by $\{\pi_{jk}\}$ which determines the prior probability of each linear combination.

Notation: As usual, $\mathcal{N}(\mathbf{x}|\boldsymbol{\mu}, \boldsymbol{\Sigma})$ denotes the multivariate Gaussian density function with center $\boldsymbol{\mu}$ and covariance matrix $\boldsymbol{\Sigma}$. Let $\mathbf{A} \in \mathbb{R}^{m \times n}$ be a matrix with m rows and n columns. The Hadamard product of two matrices (elementwise multiplication) is denoted by \circ . $(\mathbf{A})_{jk}$ denotes the element at the j th row and k th column of matrix \mathbf{A} . $(\mathbf{A})_j$ denotes the j th row of \mathbf{A} transposed (treating \mathbf{A} as a vector), i.e. for $\mathbf{A} = [\mathbf{a}_1, \dots, \mathbf{a}_n]^T$, $(\mathbf{A})_j = \mathbf{a}_j$. $\text{vec}(\mathbf{A})$ denotes the vectorization of \mathbf{A} , i.e. concatenating the columns of \mathbf{A} . $\delta_{jk} = 1$ when $j = k$ and 0 otherwise. $\mathbb{E}_{\mathbf{x}}(f(\mathbf{x}))$ is the expected value of $f(\mathbf{x})$ given random variable \mathbf{x} . We use $i = \sqrt{-1}$ instead of j as an index throughout the paper.

2 Mathematical Preliminaries

2.1 Linear combination of GMM random variables

To use the Gaussian mixture model to model endmember variability, we start by assuming that \mathbf{m}_{n_j} follows a Gaussian mixture model (GMM) and the noise also follows a Gaussian distribution. The distribution of \mathbf{y}_n is obtained using the following theorem.

Theorem 1. *If the random variable \mathbf{m}_{n_j} has a density function*

$$p(\mathbf{m}_{n_j}|\boldsymbol{\Theta}) := f_{\mathbf{m}_j}(\mathbf{m}_{n_j}) = \sum_{k=1}^{K_j} \pi_{jk} \mathcal{N}(\mathbf{m}_{n_j}|\boldsymbol{\mu}_{jk}, \boldsymbol{\Sigma}_{jk}), \quad (4)$$

s.t. $\pi_{jk} \geq 0$, $\sum_{k=1}^{K_j} \pi_{jk} = 1$, with K_j being the number of components, π_{jk} ($\boldsymbol{\mu}_{jk} \in \mathbb{R}^B$ or $\boldsymbol{\Sigma}_{jk} \in \mathbb{R}^{B \times B}$) being the weight (mean or covariance matrix) of its k th Gaussian component, $\boldsymbol{\Theta} := \{\pi_{jk}, \boldsymbol{\mu}_{jk}, \boldsymbol{\Sigma}_{jk} : j = 1, \dots, M, k = 1, \dots, K_j\}$, $\{\mathbf{m}_{n_j} : j = 1, \dots, M\}$ are independent, and the

random variable \mathbf{n}_n has a density function $p(\mathbf{n}_n) := \mathcal{N}(\mathbf{n}_n | \mathbf{0}, \mathbf{D})$, then the density function of \mathbf{y}_n given by the r.v.t. $\mathbf{y}_n = \sum_{j=1}^M \mathbf{m}_{nj} \alpha_{nj} + \mathbf{n}_n$ is another GMM

$$p(\mathbf{y}_n | \boldsymbol{\alpha}_n, \boldsymbol{\Theta}, \mathbf{D}) = \sum_{\mathbf{k} \in \mathcal{K}} \pi_{\mathbf{k}} \mathcal{N}(\mathbf{y}_n | \boldsymbol{\mu}_{n\mathbf{k}}, \boldsymbol{\Sigma}_{n\mathbf{k}}), \quad (5)$$

where $\mathcal{K} := \{1, \dots, K_1\} \times \{1, \dots, K_2\} \times \dots \times \{1, \dots, K_M\}$ is the Cartesian product of the M index sets, $\mathbf{k} := (k_1, \dots, k_M) \in \mathcal{K}$, $\pi_{\mathbf{k}} \in \mathbb{R}$, $\boldsymbol{\mu}_{n\mathbf{k}} \in \mathbb{R}^B$, $\boldsymbol{\Sigma}_{n\mathbf{k}} \in \mathbb{R}^{B \times B}$ are defined by

$$\pi_{\mathbf{k}} := \prod_{j=1}^M \pi_{jk_j}, \quad \boldsymbol{\mu}_{n\mathbf{k}} := \sum_{j=1}^M \alpha_{nj} \boldsymbol{\mu}_{jk_j}, \quad \boldsymbol{\Sigma}_{n\mathbf{k}} := \sum_{j=1}^M \alpha_{nj}^2 \boldsymbol{\Sigma}_{jk_j} + \mathbf{D}. \quad (6)$$

The proof is detailed using a characteristic function (c.f.) approach.

We first consider the distribution of the intermediate variable $\mathbf{z}_n = \sum_{j=1}^M \mathbf{m}_{nj} \alpha_{nj}$. The c.f. of $f_{\mathbf{m}_j}$ in (4), $\phi_{\mathbf{m}_j}(\mathbf{t}) : \mathbb{R}^B \rightarrow \mathbb{C}$, is given by

$$\begin{aligned} \phi_{\mathbf{m}_j}(\mathbf{t}) &= \mathbb{E}_{\mathbf{m}_j} \left(e^{i\mathbf{t}^T \mathbf{x}} \right) = \int_{\mathbb{R}^B} e^{i\mathbf{t}^T \mathbf{x}} f_{\mathbf{m}_j}(\mathbf{x}) d\mathbf{x} \\ &= \sum_{k=1}^{K_j} \pi_{jk} \int_{\mathbb{R}^B} e^{i\mathbf{t}^T \mathbf{x}} \mathcal{N}(\mathbf{x} | \boldsymbol{\mu}_{jk}, \boldsymbol{\Sigma}_{jk}) d\mathbf{x} \\ &= \sum_{k=1}^{K_j} \pi_{jk} \phi_{jk}(\mathbf{t}), \end{aligned} \quad (7)$$

where $\phi_{jk}(\mathbf{t})$ denotes the c.f. of the Gaussian distribution $\mathcal{N}(\mathbf{x} | \boldsymbol{\mu}_{jk}, \boldsymbol{\Sigma}_{jk})$ as

$$\phi_{jk}(\mathbf{t}) := \exp \left(i\mathbf{t}^T \boldsymbol{\mu}_{jk} - \frac{1}{2} \mathbf{t}^T \boldsymbol{\Sigma}_{jk} \mathbf{t} \right). \quad (8)$$

Assuming $\mathbf{m}_{n1}, \dots, \mathbf{m}_{nM}$ are independent, we can obtain the c.f. of the linear combination of these \mathbf{m}_{nj} by multiplying (7) as

$$\begin{aligned} \phi_{\mathbf{z}_n}(\mathbf{t}) &= \phi_{\mathbf{m}_{n1} \alpha_{n1} + \dots + \mathbf{m}_{nM} \alpha_{nM}}(\mathbf{t}) = \prod_{j=1}^M \phi_{\mathbf{m}_j}(\alpha_{nj} \mathbf{t}) \\ &= \sum_{k_1=1}^{K_1} \dots \sum_{k_M=1}^{K_M} \pi_{1k_1} \dots \pi_{Mk_M} \phi_{1k_1}(\alpha_{n1} \mathbf{t}) \dots \phi_{Mk_M}(\alpha_{nM} \mathbf{t}). \end{aligned}$$

Let \mathcal{K} , \mathbf{k} , $\pi_{\mathbf{k}}$ be defined as in Theorem 1. We can write the above multiple summations in an elegant way:

$$\phi_{\mathbf{z}_n}(\mathbf{t}) = \sum_{\mathbf{k} \in \mathcal{K}} \pi_{\mathbf{k}} \phi_{n\mathbf{k}}(\mathbf{t}), \quad (9)$$

where $\pi_{\mathbf{k}} \geq 0$, $\sum_{\mathbf{k} \in \mathcal{K}} \pi_{\mathbf{k}} = 1$ and

$$\begin{aligned} \phi_{n\mathbf{k}}(\mathbf{t}) &:= \phi_{1k_1}(\alpha_{n1} \mathbf{t}) \dots \phi_{Mk_M}(\alpha_{nM} \mathbf{t}) \\ &= \exp \left\{ i\mathbf{t}^T \left(\sum_{j=1}^M \alpha_{nj} \boldsymbol{\mu}_{jk_j} \right) - \frac{1}{2} \mathbf{t}^T \left(\sum_{j=1}^M \alpha_{nj}^2 \boldsymbol{\Sigma}_{jk_j} \right) \mathbf{t} \right\}, \end{aligned}$$

where (8) is used. Since $\phi_{n\mathbf{k}}(\mathbf{t})$ also has a form of c.f. of a Gaussian distribution, the corresponding distribution turns out to be $\mathcal{N}\left(\mathbf{x}|\sum_j \alpha_{nj}\boldsymbol{\mu}_{jk_j}, \sum_j \alpha_{nj}^2\boldsymbol{\Sigma}_{jk_j}\right)$. Hence, the distribution of \mathbf{z}_n can be obtained by the Fourier transform of (9)

$$\begin{aligned} f_{\mathbf{z}_n}(\mathbf{z}_n) &= \frac{1}{(2\pi)^B} \int_{\mathbb{R}^B} e^{-i\mathbf{t}^T \mathbf{z}_n} \phi_{\mathbf{z}_n}(\mathbf{t}) d\mathbf{t} \\ &= \frac{1}{(2\pi)^B} \int_{\mathbb{R}^B} e^{-i\mathbf{t}^T \mathbf{z}_n} \sum_{\mathbf{k} \in \mathcal{K}} \pi_{\mathbf{k}} \phi_{n\mathbf{k}}(\mathbf{t}) d\mathbf{t} \\ &= \sum_{\mathbf{k} \in \mathcal{K}} \pi_{\mathbf{k}} \mathcal{N}\left(\mathbf{z}_n \mid \sum_{j=1}^M \alpha_{nj} \boldsymbol{\mu}_{jk_j}, \sum_{j=1}^M \alpha_{nj}^2 \boldsymbol{\Sigma}_{jk_j}\right), \end{aligned} \quad (10)$$

which is still a mixture of Gaussians.

After finding the distribution of the linear combination, we can add the noise term to find the distribution of \mathbf{y}_n . Suppose the noise also follows a Gaussian distribution, $p(\mathbf{n}_n) := f_{\mathbf{n}_n}(\mathbf{n}_n) = \mathcal{N}(\mathbf{n}_n | \mathbf{0}, \mathbf{D})$, where \mathbf{D} is the noise covariance matrix. We assume that the noise at different wavelengths is independent (σ_k^2 being the noise variance of the k th band), i.e. $\mathbf{D} = \text{diag}(\sigma_1^2, \sigma_2^2, \dots, \sigma_B^2) \in \mathbb{R}^{B \times B}$ (if it is not independent, the noise can actually be easily whitened to be independent as in [24]). Its c.f. has the following form

$$\phi_{\mathbf{n}_n}(\mathbf{t}) = \exp\left(-\frac{1}{2}\mathbf{t}^T \mathbf{D} \mathbf{t}\right) \quad (11)$$

by (8). Then the c.f. of \mathbf{y}_n can be obtained by multiplying (9) and (11) (as \mathbf{z}_n and \mathbf{n}_n are independent)

$$\begin{aligned} \phi_{\mathbf{y}_n}(\mathbf{t}) &= \phi_{\mathbf{z}_n}(\mathbf{t}) \phi_{\mathbf{n}_n}(\mathbf{t}) = \sum_{\mathbf{k} \in \mathcal{K}} \pi_{\mathbf{k}} \phi_{n\mathbf{k}}(\mathbf{t}) \phi_{n\mathbf{k}}(\mathbf{t}) \\ &= \sum_{\mathbf{k} \in \mathcal{K}} \pi_{\mathbf{k}} \exp\left\{i\mathbf{t}^T \boldsymbol{\mu}_{n\mathbf{k}} - \frac{1}{2}\mathbf{t}^T \boldsymbol{\Sigma}_{n\mathbf{k}} \mathbf{t}\right\}, \end{aligned}$$

where $\boldsymbol{\mu}_{n\mathbf{k}}$ and $\boldsymbol{\Sigma}_{n\mathbf{k}}$ are defined in (6). Finally, the distribution of \mathbf{y} can be shown to be (5) by the Fourier transform again as in (10).

If $\mathcal{K} = \{1\} \times \{1\} \times \dots \times \{1\}$, i.e. each endmember has only one Gaussian component, we have $\pi_{11} = 1, \dots, \pi_{M1} = 1$, then $\pi_{\mathbf{k}} = \pi_{11} \dots \pi_{M1} = 1$. The distribution of \mathbf{y}_n becomes

$$p(\mathbf{y}_n | \boldsymbol{\alpha}_n, \boldsymbol{\Theta}, \mathbf{D}) = \mathcal{N}\left(\mathbf{y}_n \mid \sum_{j=1}^M \alpha_{nj} \boldsymbol{\mu}_{j1}, \sum_{j=1}^M \alpha_{nj}^2 \boldsymbol{\Sigma}_{j1} + \mathbf{D}\right), \quad (12)$$

which is exactly the NCM in (3).

2.2 Another perspective

Theorem 1 obtains the density of each pixel by directly performing a r.v.t. based on the LMM, which can be used to estimate the abundances and distribution parameters. Here, we will obtain the density from another perspective, which provides a foundation to estimate the endmembers for each pixel. Again, let the noise follow the density function $p(\mathbf{n}_n) := \mathcal{N}(\mathbf{n}_n | \mathbf{0}, \mathbf{D})$. Considering

$\{\mathbf{m}_{nj}\}$ and $\{\alpha_{nj}\}$ as fixed values, the r.v.t. $\mathbf{y}_n = \sum_j \mathbf{m}_{nj}\alpha_{nj} + \mathbf{n}_n$ implies that the density of \mathbf{y}_n is given by

$$p(\mathbf{y}_n|\alpha_n, \mathbf{M}_n, \mathbf{D}) = \mathcal{N}\left(\mathbf{y}_n \mid \sum_j \mathbf{m}_{nj}\alpha_{nj}, \mathbf{D}\right) \quad (13)$$

where $\mathbf{M}_n = [\mathbf{m}_{n1}, \dots, \mathbf{m}_{nM}]^T \in \mathbb{R}^{M \times B}$ are the endmembers for the n th pixel. We have the following theorem which gives the same result as in Theorem 1.

Theorem 2. *If the random variables $\{\mathbf{m}_{nj} : j = 1, \dots, M\}$ follow GMM distributions*

$$p(\mathbf{m}_{nj}|\Theta) := \sum_{k=1}^{K_j} \pi_{jk} \mathcal{N}(\mathbf{m}_{nj} | \boldsymbol{\mu}_{jk}, \boldsymbol{\Sigma}_{jk}),$$

and they are independent, i.e.

$$p(\mathbf{M}_n|\Theta) = \prod_{j=1}^M p(\mathbf{m}_{nj}|\Theta), \quad (14)$$

then the conditional density $p(\mathbf{y}_n|\alpha_n, \Theta, \mathbf{D})$ obtained by marginalizing \mathbf{M}_n in $p(\mathbf{y}_n, \mathbf{M}_n|\alpha_n, \Theta, \mathbf{D})$ has the same form as in Theorem 1:

$$\begin{aligned} p(\mathbf{y}_n|\alpha_n, \Theta, \mathbf{D}) &= \int p(\mathbf{y}_n|\alpha_n, \mathbf{M}_n, \mathbf{D}) p(\mathbf{M}_n|\Theta) d\mathbf{M}_n \\ &= \sum_{\mathbf{k} \in \mathcal{K}} \pi_{\mathbf{k}} \mathcal{N}(\mathbf{y}_n | \boldsymbol{\mu}_{n\mathbf{k}}, \boldsymbol{\Sigma}_{n\mathbf{k}}), \end{aligned}$$

where $p(\mathbf{y}_n|\alpha_n, \mathbf{M}_n, \mathbf{D}) = \mathcal{N}\left(\mathbf{y}_n \mid \sum_j \mathbf{m}_{nj}\alpha_{nj}, \mathbf{D}\right)$.

The proof is much more complicated (in terms of algebra) and therefore relegated to the Appendix of the paper.

2.3 An example

We give an example to illustrate the basic idea of this paper. Suppose we have $M = 4$ endmembers with $K_1 = 1$, $K_2 = 2$, $K_3 = 3$, $K_4 = 1$. Their distributions follow (4) with $\boldsymbol{\mu}_{jk}, \boldsymbol{\Sigma}_{jk}$, $j = 1, 2, 3, 4$, $k = 1, \dots, K_j$. Let the weights of these components be $\pi_{11} = \pi_{41} = 1$, $\pi_{21} = 0.3$, $\pi_{22} = 0.7$, $\pi_{31} = 0.2$, $\pi_{32} = 0.4$, $\pi_{33} = 0.4$. Then, \mathcal{K} has 6 entries from the Cartesian product, $\{1\} \times \{1, 2\} \times \{1, 2, 3\} \times \{1\}$. We list the values for $\pi_{\mathbf{k}}, \boldsymbol{\mu}_{n\mathbf{k}}$ in Table 1. For example, for $\mathbf{k} = (1, 2, 3, 1)$, $\pi_{\mathbf{k}} = \pi_{11}\pi_{22}\pi_{33}\pi_{41} = 0.28$. The value of $\boldsymbol{\mu}_{n\mathbf{k}}$ is a linear combination of $\boldsymbol{\mu}_{jk}$ (pick one component for each j) based on the configuration \mathbf{k} . Hence, the distribution of \mathbf{y}_n in (5) is a Gaussian mixture of 6 components with $\pi_{\mathbf{k}}, \boldsymbol{\mu}_{n\mathbf{k}}$ given in Table 1 ($\boldsymbol{\Sigma}_{n\mathbf{k}}$ can be derived similar to $\boldsymbol{\mu}_{n\mathbf{k}}$). Recalling the intuition in Fig. 2, we will show that applying it to hyperspectral unmixing will force each pixel to match all the $\boldsymbol{\mu}_{n\mathbf{k}}$ s, but with emphasis determined by $\pi_{n\mathbf{k}}$.

3 Gaussian Mixture Model for Endmember Variability

3.1 The GMM for hyperspectral unmixing

Based on the analysis in Section 2, we can model the conditional distribution of all the pixels $\mathbf{Y} := [\mathbf{y}_1, \dots, \mathbf{y}_N]^T \in \mathbb{R}^{N \times B}$ given all the abundances $\mathbf{A} := [\alpha_1, \dots, \alpha_N]^T \in \mathbb{R}^{N \times M}$ ($\alpha_n :=$

Table 1: Values for the various quantities in the simple example.

\mathbf{k}	$\pi_{\mathbf{k}}$	$\boldsymbol{\mu}_{n\mathbf{k}}$ in (6)
(1, 1, 1, 1)	0.06	$\alpha_{n1}\boldsymbol{\mu}_{11} + \alpha_{n2}\boldsymbol{\mu}_{21} + \alpha_{n3}\boldsymbol{\mu}_{31} + \alpha_{n4}\boldsymbol{\mu}_{41}$
(1, 2, 1, 1)	0.14	$\alpha_{n1}\boldsymbol{\mu}_{11} + \alpha_{n2}\boldsymbol{\mu}_{22} + \alpha_{n3}\boldsymbol{\mu}_{31} + \alpha_{n4}\boldsymbol{\mu}_{41}$
(1, 1, 2, 1)	0.12	$\alpha_{n1}\boldsymbol{\mu}_{11} + \alpha_{n2}\boldsymbol{\mu}_{21} + \alpha_{n3}\boldsymbol{\mu}_{32} + \alpha_{n4}\boldsymbol{\mu}_{41}$
(1, 2, 2, 1)	0.28	$\alpha_{n1}\boldsymbol{\mu}_{11} + \alpha_{n2}\boldsymbol{\mu}_{22} + \alpha_{n3}\boldsymbol{\mu}_{32} + \alpha_{n4}\boldsymbol{\mu}_{41}$
(1, 1, 3, 1)	0.12	$\alpha_{n1}\boldsymbol{\mu}_{11} + \alpha_{n2}\boldsymbol{\mu}_{21} + \alpha_{n3}\boldsymbol{\mu}_{33} + \alpha_{n4}\boldsymbol{\mu}_{41}$
(1, 2, 3, 1)	0.28	$\alpha_{n1}\boldsymbol{\mu}_{11} + \alpha_{n2}\boldsymbol{\mu}_{22} + \alpha_{n3}\boldsymbol{\mu}_{33} + \alpha_{n4}\boldsymbol{\mu}_{41}$

$[\alpha_{n1}, \dots, \alpha_{nM}]^T$) and GMM parameters, which leads to a maximum *a posteriori* (MAP) problem. Using the result in (5) and assuming the conditional distributions of \mathbf{y}_n are independent, the distribution of \mathbf{Y} given $\mathbf{A}, \boldsymbol{\Theta}, \mathbf{D}$ becomes

$$p(\mathbf{Y}|\mathbf{A}, \boldsymbol{\Theta}, \mathbf{D}) = \prod_{n=1}^N p(\mathbf{y}_n|\boldsymbol{\alpha}_n, \boldsymbol{\Theta}, \mathbf{D}). \quad (15)$$

Based on the hyperspectral unmixing context, we can set the priors for \mathbf{A} . Suppose we use the same prior on \mathbf{A} as in [25], i.e.

$$\begin{aligned} p(\mathbf{A}) &\propto \exp\left\{-\frac{\beta_1}{2}\text{Tr}(\mathbf{A}^T\mathbf{L}\mathbf{A}) + \frac{\beta_2}{2}\text{Tr}(\mathbf{A}^T\mathbf{A})\right\} \\ &= \exp\left\{-\frac{\beta_1}{2}\text{Tr}(\mathbf{A}^T\mathbf{K}\mathbf{A})\right\}, \end{aligned} \quad (16)$$

where \mathbf{L} is a *graph Laplacian* matrix constructed from w_{nm} , $n, m = 1, \dots, N$ with $w_{nm} = e^{-\|\mathbf{y}_n - \mathbf{y}_m\|^2/2B\eta^2}$ for neighboring pixels and 0 otherwise. We have $\text{Tr}(\mathbf{A}^T\mathbf{L}\mathbf{A}) = \frac{1}{2}\sum_{n,m} w_{nm}\|\boldsymbol{\alpha}_n - \boldsymbol{\alpha}_m\|^2$, $\mathbf{K} = \mathbf{L} - \frac{\beta_2}{\beta_1}\mathbf{I}_N$ (suppose $\beta_1 \neq 0$) with β_1 controlling smoothness and β_2 controlling sparsity of the abundance maps.

From the conditional density function and the priors, Bayes' theorem says the posterior is given by

$$p(\mathbf{A}, \boldsymbol{\Theta}|\mathbf{Y}, \mathbf{D}) \propto p(\mathbf{Y}|\mathbf{A}, \boldsymbol{\Theta}, \mathbf{D})p(\mathbf{A})p(\boldsymbol{\Theta}), \quad (17)$$

where $p(\mathbf{Y})$, $p(\boldsymbol{\Theta})$ are assumed to follow uniform distributions. Maximizing $p(\mathbf{A}, \boldsymbol{\Theta}|\mathbf{Y}, \mathbf{D})$ is equivalent to minimizing $-\log p(\mathbf{A}, \boldsymbol{\Theta}|\mathbf{Y}, \mathbf{D})$, which reduces to the following form by combining (5), (15), (16) and (17):

$$\mathcal{E}(\mathbf{A}, \boldsymbol{\Theta}) = -\sum_{n=1}^N \log \sum_{\mathbf{k} \in \mathcal{K}} \pi_{\mathbf{k}} \mathcal{N}(\mathbf{y}_n|\boldsymbol{\mu}_{n\mathbf{k}}, \boldsymbol{\Sigma}_{n\mathbf{k}}) + \mathcal{E}_{\text{prior}}(\mathbf{A}), \quad (18)$$

$$\text{s.t. } \pi_{\mathbf{k}} \geq 0, \sum_{\mathbf{k} \in \mathcal{K}} \pi_{\mathbf{k}} = 1, \alpha_{nj} \geq 0, \sum_{j=1}^M \alpha_{nj} = 1, \forall n$$

where $\mathcal{E}_{\text{prior}}(\mathbf{A}) = \frac{\beta_1}{2}\text{Tr}(\mathbf{A}^T\mathbf{K}\mathbf{A})$, and $\boldsymbol{\mu}_{n\mathbf{k}}, \boldsymbol{\Sigma}_{n\mathbf{k}}$ are defined in (6).

3.2 Relationships to least-squares, NCM and MESMA

Let us focus on the first term in (18) and call it the *data fidelity term*. We can relate it to NCM and the least-squares term $\sum_n \|\mathbf{y}_n - \sum_j \alpha_{nj} \mathbf{m}_j\|^2$ as used in previous research. The data fidelity term in NCM follows (3) and is based on minimizing the negative log-likelihood

$$-\log p(\mathbf{Y}) = -\log \prod_{n=1}^N p(\mathbf{y}_n) = -\sum_{n=1}^N \log \mathcal{N}(\mathbf{y}_n | \boldsymbol{\mu}_{n\mathbf{1}}, \boldsymbol{\Sigma}_{n\mathbf{1}}) \quad (19)$$

by assuming \mathbf{y}_n s are independent, where $\boldsymbol{\mu}_{n\mathbf{1}} := \sum_j \alpha_{nj} \boldsymbol{\mu}_j$, $\boldsymbol{\Sigma}_{n\mathbf{1}} := \sum_j \alpha_{nj}^2 \boldsymbol{\Sigma}_j + \sigma^2 \mathbf{I}_B$. Expanding (19) using the form of the Gaussian distribution leads to the objective function

$$\sum_{n=1}^N \log |\boldsymbol{\Sigma}_{n\mathbf{1}}| + \sum_{n=1}^N (\mathbf{y}_n - \boldsymbol{\mu}_{n\mathbf{1}})^T \boldsymbol{\Sigma}_{n\mathbf{1}}^{-1} (\mathbf{y}_n - \boldsymbol{\mu}_{n\mathbf{1}}). \quad (20)$$

We can see that the least-squares minimization is a special case of NCM with $\boldsymbol{\Sigma}_j \ll \sigma^2 \mathbf{I}_B$, i.e. when there is little endmember variability.

The proposed GMM further generalizes NCM from a statistical perspective. Since π_{jk} represents the prior probability of the latent variable in a GMM, $\pi_{\mathbf{k}}$ represents the prior probability of picking a combination. If we see \mathbf{k} as a (discrete) random variable whose sample space is \mathcal{K} , (5) can be seen as

$$p(\mathbf{y}_n | \boldsymbol{\alpha}_n, \boldsymbol{\Theta}, \mathbf{D}) = \sum_{\mathbf{k} \in \mathcal{K}} p(\mathbf{k}) p(\mathbf{y}_n | \mathbf{k}, \boldsymbol{\alpha}_n, \boldsymbol{\Theta}, \mathbf{D}),$$

where $p(\mathbf{k}) = \pi_{\mathbf{k}}$ and $p(\mathbf{y}_n | \mathbf{k}, \boldsymbol{\alpha}_n, \boldsymbol{\Theta}, \mathbf{D}) = \mathcal{N}(\mathbf{y}_n | \boldsymbol{\mu}_{n\mathbf{k}}, \boldsymbol{\Sigma}_{n\mathbf{k}})$. From this perspective, each pixel is generated by first sampling \mathbf{k} , then sampling a Gaussian distribution determined by $\mathbf{k}, \boldsymbol{\Theta}$. Unlike NCM that tries to make each \mathbf{y}_n close to $\boldsymbol{\mu}_{n\mathbf{1}}$ which is a linear combination of a fixed set $\{\boldsymbol{\mu}_j\}$, GMM further generalizes it by trying to make \mathbf{y}_n close to every $\boldsymbol{\mu}_{n\mathbf{k}}$ which are all the possible linear combinations of $\{\boldsymbol{\mu}_{jk}\}$. It makes sense that the summation in (18) is weighted by $\pi_{\mathbf{k}}$ in a way that if one combination has a high probability to appear, i.e. $\pi_{\mathbf{k}}$ is larger for a certain \mathbf{k} , the effort is biased to make \mathbf{y}_n closer to this particular $\boldsymbol{\mu}_{n\mathbf{k}}$. Fig. 2 shows the differences among these.

The widely adopted MESMA takes a library of endmember spectra as input, tries all the combinations and pick the combination with least reconstruction error. The philosophy is similar to our model despite the fundamental difference that MESMA is explicit whereas we are implicit in terms of linear combinations. Compared to MESMA, the GMM approach separates the library into M groups where each group represents a material and is clustered into several centers, such that the combination can only take place by picking one center from each group. Also, the size of each cluster affects the probability of picking its center. Hence, our model can adapt to very large library sizes as long as the number of clusters does not increase too much.

3.3 Optimization

Estimating the parameters of GMMs has been studied extensively, from early expectation maximization (EM) from the statistical community to projection based clustering from the computer science community [26, 27]. There are simple and deterministic algorithms, which usually require the centers of Gaussian be separable. However, we face a more challenging problem since each pixel is generated by a different GMM determined by the coefficients $\boldsymbol{\alpha}_n$. Since EM can be seen as a special case of Majorization-Minimization algorithms, which is more flexible, we adopt this approach. Considering that we have too many parameters $\mathbf{A}, \boldsymbol{\Theta}$ to update in the M step, they

are updated sequentially as long as the complete data log-likelihood increases. This is also called *generalized expectation maximization* (GEM) [28].

Following the routine of EM, the E step calculates the posterior probability of the latent variable given the observed data and old parameters

$$\gamma_{n\mathbf{k}} = \frac{\pi_{\mathbf{k}} \mathcal{N}(\mathbf{y}_n | \boldsymbol{\mu}_{n\mathbf{k}}, \boldsymbol{\Sigma}_{n\mathbf{k}})}{\sum_{\mathbf{k} \in \mathcal{K}} \pi_{\mathbf{k}} \mathcal{N}(\mathbf{y}_n | \boldsymbol{\mu}_{n\mathbf{k}}, \boldsymbol{\Sigma}_{n\mathbf{k}})}. \quad (21)$$

The M step usually maximizes the expected value of the complete data log-likelihood. Here, we have priors in the Bayesian formulation. Hence, we need to minimize

$$\mathcal{E}_M = - \sum_{n=1}^N \sum_{\mathbf{k} \in \mathcal{K}} \gamma_{n\mathbf{k}} \{ \log \pi_{\mathbf{k}} + \log \mathcal{N}(\mathbf{y}_n | \boldsymbol{\mu}_{n\mathbf{k}}, \boldsymbol{\Sigma}_{n\mathbf{k}}) \} + \mathcal{E}_{\text{prior}}. \quad (22)$$

This leads to a common update step for $\pi_{\mathbf{k}}$ as

$$\pi_{\mathbf{k}} = \frac{1}{N} \sum_{n=1}^N \gamma_{n\mathbf{k}}. \quad (23)$$

We now focus on updating $\{\boldsymbol{\mu}_{jk}, \boldsymbol{\Sigma}_{jk}\}$ and \mathbf{A} . To achieve this, we require the derivatives of \mathcal{E}_M in (22) w.r.t. $\boldsymbol{\mu}_{jk}, \boldsymbol{\Sigma}_{jk}, \alpha_{nj}$. After some tedious algebra using (6), we get

$$\frac{\partial \mathcal{E}_M}{\partial \boldsymbol{\mu}_{jl}} = - \sum_{n=1}^N \sum_{\mathbf{k} \in \mathcal{K}} \delta_{lk_j} \alpha_{nj} \boldsymbol{\lambda}_{n\mathbf{k}} \quad (24)$$

$$\frac{\partial \mathcal{E}_M}{\partial \boldsymbol{\Sigma}_{jl}} = - \sum_{n=1}^N \sum_{\mathbf{k} \in \mathcal{K}} \delta_{lk_j} \alpha_{nj}^2 \boldsymbol{\Psi}_{n\mathbf{k}}, \quad (25)$$

$$\begin{aligned} \frac{\partial \mathcal{E}_M}{\partial \alpha_{nj}} &= - \sum_{\mathbf{k} \in \mathcal{K}} \boldsymbol{\lambda}_{n\mathbf{k}}^T \boldsymbol{\mu}_{jk_j} - 2\alpha_{nj} \sum_{\mathbf{k} \in \mathcal{K}} \text{Tr}(\boldsymbol{\Psi}_{n\mathbf{k}}^T \boldsymbol{\Sigma}_{jk_j}) \\ &\quad + \beta_1 (\mathbf{KA})_{nj}, \end{aligned} \quad (26)$$

where $\boldsymbol{\lambda}_{n\mathbf{k}} \in \mathbb{R}^{B \times 1}$ and $\boldsymbol{\Psi}_{n\mathbf{k}} \in \mathbb{R}^{B \times B}$ are given by

$$\boldsymbol{\lambda}_{n\mathbf{k}} = \gamma_{n\mathbf{k}} \boldsymbol{\Sigma}_{n\mathbf{k}}^{-1} (\mathbf{y}_n - \boldsymbol{\mu}_{n\mathbf{k}}), \quad (27)$$

$$\boldsymbol{\Psi}_{n\mathbf{k}} = \frac{1}{2} \gamma_{n\mathbf{k}} \boldsymbol{\Sigma}_{n\mathbf{k}}^{-T} (\mathbf{y}_n - \boldsymbol{\mu}_{n\mathbf{k}}) (\mathbf{y}_n - \boldsymbol{\mu}_{n\mathbf{k}})^T \boldsymbol{\Sigma}_{n\mathbf{k}}^{-T} - \frac{1}{2} \gamma_{n\mathbf{k}} \boldsymbol{\Sigma}_{n\mathbf{k}}^{-T}. \quad (28)$$

It is better to represent the derivatives in matrix forms for the sake of implementation convenience. Considering the multiple summations in (24), (25) and (26), we can write them as

$$\frac{\partial \mathcal{E}_M}{\partial \boldsymbol{\mu}_{jl}} = - \sum_{\mathbf{k} \in \mathcal{K}} \delta_{lk_j} (\mathbf{A}^T \boldsymbol{\Lambda}_{\mathbf{k}})_j, \quad (29)$$

$$\frac{\partial \mathcal{E}_M}{\partial \text{vec}(\boldsymbol{\Sigma}_{jl})} = - \sum_{\mathbf{k} \in \mathcal{K}} \delta_{lk_j} \left((\mathbf{A} \circ \mathbf{A})^T \boldsymbol{\Psi}_{\mathbf{k}} \right)_j, \quad (30)$$

$$\frac{\partial \mathcal{E}_M}{\partial \mathbf{A}} = - \sum_{\mathbf{k} \in \mathcal{K}} \boldsymbol{\Lambda}_{\mathbf{k}} \mathbf{R}_{\mathbf{k}}^T - 2\mathbf{A} \circ \sum_{\mathbf{k} \in \mathcal{K}} \boldsymbol{\Psi}_{\mathbf{k}} \mathbf{S}_{\mathbf{k}}^T + \beta_1 \mathbf{KA}, \quad (31)$$

where $\mathbf{\Lambda}_{\mathbf{k}} \in \mathbb{R}^{N \times B}$, $\mathbf{\Psi}_{\mathbf{k}} \in \mathbb{R}^{N \times B^2}$ denote the matrices formed by $\{\boldsymbol{\lambda}_{n\mathbf{k}}, \boldsymbol{\Psi}_{n\mathbf{k}}\}$ as follows

$$\mathbf{\Lambda}_{\mathbf{k}} := [\boldsymbol{\lambda}_{1\mathbf{k}}, \boldsymbol{\lambda}_{2\mathbf{k}}, \dots, \boldsymbol{\lambda}_{N\mathbf{k}}]^T,$$

$$\mathbf{\Psi}_{\mathbf{k}} := [\text{vec}(\boldsymbol{\Psi}_{1\mathbf{k}}), \text{vec}(\boldsymbol{\Psi}_{2\mathbf{k}}), \dots, \text{vec}(\boldsymbol{\Psi}_{N\mathbf{k}})]^T,$$

and $\mathbf{R}_{\mathbf{k}} \in \mathbb{R}^{M \times B}$, $\mathbf{S}_{\mathbf{k}} \in \mathbb{R}^{M \times B^2}$ are defined by

$$\mathbf{R}_{\mathbf{k}} := [\boldsymbol{\mu}_{1k_1}, \boldsymbol{\mu}_{2k_2}, \dots, \boldsymbol{\mu}_{Mk_M}]^T, \quad (32)$$

$$\mathbf{S}_{\mathbf{k}} := [\text{vec}(\boldsymbol{\Sigma}_{1k_1}), \text{vec}(\boldsymbol{\Sigma}_{2k_2}), \dots, \text{vec}(\boldsymbol{\Sigma}_{Mk_M})]^T. \quad (33)$$

The minimum of \mathcal{E}_M corresponds to $\frac{\partial \mathcal{E}_M}{\partial \boldsymbol{\mu}_{jl}} = 0$, $\frac{\partial \mathcal{E}_M}{\partial \boldsymbol{\Sigma}_{jl}} = 0$, and $\frac{\partial \mathcal{E}_M}{\partial \mathbf{A}} = 0$ if the optimization problem is unconstrained. However, since we have the non-negativity and sum-to-one constraint to α_{nj} and positive definite constraint of $\boldsymbol{\Sigma}_{jk}$, minimizing \mathcal{E}_M is very difficult. Therefore, in each M step, we only decrease this objective function by *projected gradient descent* (please see Section 2.3 in [29], [30]) using (29), (30) and (31), where the projection functions for \mathbf{A} and $\{\boldsymbol{\Sigma}_{jk}\}$ are the same as in [25].

Finally, from the estimated $\pi_{\mathbf{k}}$, we can recover the sets of weights as $\pi_{jl} = \sum_{\mathbf{k} \in \mathcal{K}} \delta_{lk_j} \pi_{\mathbf{k}}$.

3.4 Model selection

The number of components K_j can be specified or estimated from the data. For the latter case, we have some pure pixels and estimate K_j by deploying a standard model selection method. Suppose we have N_j pure pixels $\mathbf{Y}_j := [\mathbf{y}_1^j, \mathbf{y}_2^j, \dots, \mathbf{y}_{N_j}^j]^T \in \mathbb{R}^{N_j \times B}$ for the j th endmember, $f_{\mathbf{m}_j}(\mathbf{y}|\boldsymbol{\Theta}_j)$ is the estimated density function with $\boldsymbol{\Theta}_j := \{\pi_{jk}, \boldsymbol{\mu}_{jk}, \boldsymbol{\Sigma}_{jk} : k = 1, \dots, K_j\}$, $g_{\mathbf{m}_j}(\mathbf{y})$ is the true density function. The information criterion based model selection approach tries to find K_j that minimizes their difference, e.g. the Kullback-Leibler (KL) divergence

$$\begin{aligned} \mathcal{D}_{\text{KL}}(g_{\mathbf{m}_j} \| f_{\mathbf{m}_j}) &= \int_{\mathbb{R}^B} g_{\mathbf{m}_j}(\mathbf{y}) \log \frac{g_{\mathbf{m}_j}(\mathbf{y})}{f_{\mathbf{m}_j}(\mathbf{y}|\boldsymbol{\Theta}_j)} d\mathbf{y} \\ &\approx -\frac{1}{N_j} \sum_{n=1}^{N_j} \log f_{\mathbf{m}_j}(\mathbf{y}_n^j | \boldsymbol{\Theta}_j) + \text{const}, \end{aligned}$$

where the approximation of $\int g_{\mathbf{m}_j}(\mathbf{y}) \log f_{\mathbf{m}_j}(\mathbf{y}|\boldsymbol{\Theta}_j) d\mathbf{y}$ by the log-likelihood is usually biased as the empirical distribution function is closer to the fitted distribution than the true one. Akaike's information criterion is one way to approximate the bias. Here, we use the cross-validation-based information criterion (CVIC) to correct for the bias [31, 32]. Let

$$\mathcal{L}_{\mathbf{Y}_j}(\boldsymbol{\Theta}_j) = \sum_{n=1}^{N_j} \log f_{\mathbf{m}_j}(\mathbf{y}_n^j | \boldsymbol{\Theta}_j). \quad (34)$$

The V -fold cross validation (we use $V = 5$ here) divides the input set \mathbf{Y}_j into V subsets $\{\mathbf{Y}_j^1, \mathbf{Y}_j^2, \dots, \mathbf{Y}_j^V\}$ with equal sizes. Then for each subset \mathbf{Y}_j^v , $v = 1, \dots, V$, the remaining data are used to replace \mathbf{Y}_j in (34) such that (34) is maximized by $\boldsymbol{\Theta}_j^v$. Then $\mathcal{L}_{K_j} = \sum_v \mathcal{L}_{\mathbf{Y}_j^v}(\boldsymbol{\Theta}_j^v)$ is evaluated and the optimal $\hat{K}_j = \arg \max_{K_j} \mathcal{L}_{K_j}$.

3.5 Implementation details

The algorithm can be implemented in a supervised or unsupervised manner. In both cases, because of the large computational cost, we project the pixel data to a low dimensional space by principal component analysis (PCA) and perform the optimization, the result then projected back to the original space. Let $\mathbf{E} \in \mathbb{R}^{B \times d}$ be the projection matrix and $\mathbf{c} \in \mathbb{R}^B$ be the translation vector, then

$$\mathbf{E}^T (\mathbf{y}_n - \mathbf{c}) = \sum_{j=1}^M \mathbf{E}^T (\mathbf{m}_{nj} - \mathbf{c}) \alpha_{nj} + \mathbf{E}^T \mathbf{n}_n.$$

This means that for the projected pixels, the j th endmember $\mathbf{m}'_{nj} = \mathbf{E}^T (\mathbf{m}_{nj} - \mathbf{c})$ follows a distribution

$$p(\mathbf{m}'_{nj} | \Theta) = \sum_{k=1}^{K_j} \pi_{jk} \mathcal{N}(\mathbf{m}'_{nj} | \mathbf{E}^T (\boldsymbol{\mu}_{jk} - \mathbf{c}), \mathbf{E}^T \boldsymbol{\Sigma}_{jk} \mathbf{E})$$

and the noise $\mathbf{n}'_n = \mathbf{E}^T \mathbf{n}_n$ follows $\mathcal{N}(\mathbf{n}'_n | \mathbf{0}, \mathbf{E}^T \mathbf{D} \mathbf{E})$.

In the supervised unmixing scenario, we assume the endmember spectra are known. After estimating the number of components following Section 3.4, and calculating Θ using the standard EM algorithm, we only need to update γ_{nk} by (21) and \mathbf{A} by (31) with $\pi_{\mathbf{k}}$, $\boldsymbol{\mu}_{jk}$ and $\boldsymbol{\Sigma}_{jk}$ fixed. The initialization of \mathbf{A} can utilize the multiple combinations of means. For each α_n , we first set $\alpha_{nk} \leftarrow (\mathbf{R}_{\mathbf{k}} \mathbf{R}_{\mathbf{k}}^T + \epsilon \mathbf{I}_M)^{-1} \mathbf{R}_{\mathbf{k}} \mathbf{y}_n$, then project it to the simplex space, and finally set $\alpha_n \leftarrow \alpha_{n\hat{\mathbf{k}}}$ with $\hat{\mathbf{k}} = \arg \min_{\mathbf{k}} \|\mathbf{y}_n - \mathbf{R}_{\mathbf{k}}^T \alpha_{nk}\|^2$, i.e. choose the α_{nk} that minimizes the reconstruction error.

In the unsupervised unmixing scenario, we will assume the resolution is high enough such that the hyperspectral image can be segmented into several regions where the interior pixels in each region are pure pixels. The optimization is performed in several steps, where we first obtain a segmentation result, then use CVIC to determine the number of components, and finally estimate \mathbf{A} with Θ fixed. The details are given as follows.

Step 1: Initialization. We start with $K_j = 1, \forall j$ and use K-means to find the initial means \mathbf{R}_1 . The initial \mathbf{A} is set to $\mathbf{A} \leftarrow \mathbf{Y} \mathbf{R}_1^T (\mathbf{R}_1 \mathbf{R}_1^T + \epsilon \mathbf{I}_M)^{-1}$ (by minimizing $\|\mathbf{Y} - \mathbf{A} \mathbf{R}_1\|_F^2$), then projected to the valid simplex space as in [25]. The initial covariance matrices are set to $\boldsymbol{\Sigma}_{j1} \leftarrow 0.1^2 \mathbf{I}_B, \forall j$. For the noise matrix \mathbf{D} , although there is research focused on noise estimation [33, 34], endmember variability was not considered and validation was performed only for the simple LMM assumption. Hence, we use an empirical value $\mathbf{D} = 0.001^2 \mathbf{I}_B$, which is usually much less than the variability of covariance matrices in (6).

Step 2: Segmentation. Given the initial conditions, we use the GEM algorithm to iteratively update γ_{nk} by (21), $\pi_{\mathbf{k}}$ by (23), $\boldsymbol{\mu}_{jk}$ by (29), \mathbf{A} by (31) while keeping $\boldsymbol{\Sigma}_{jk}$ fixed. For γ_{nk} and $\pi_{\mathbf{k}}$, a direct update equation is available. For $\boldsymbol{\mu}_{jk}$, we can use gradient descent. For \mathbf{A} , since we have the non-negativity and sum-to-one constraints, a projected gradient descent similar to the one used in [25] can be applied. To ensure a segmentation effect, a large β_2 is used in this step.

Step 3: Model selection and abundance estimation. Using the segmentation-like abundance maps from the previous step, we can obtain the interior pixels \mathbf{Y}_j by thresholding the abundances (e.g. $\alpha_{nj} > 0.99$) and performing image erosion to trim the boundaries with structure element size r_{se} . Following Section 3.4, we can determine the number of components K_j and further calculate Θ_j by standard EM. Since β_2 is relatively large in the previous step, it is reduced by $\beta_2 \leftarrow \zeta \beta_2$ where $\zeta = 0.05$. Then we restart the optimization to estimate the abundances with Θ fixed.

3.6 Estimation of endmembers for each pixel

While the previous sections discuss the estimation of the abundances and endmember distribution parameters, they do not actually estimate the endmembers $\{\mathbf{m}_{nj} : n = 1, \dots, N, j = 1, \dots, M\}$ for each pixel. In this Section, we will discuss this additional problem and note its absence in the previous NCM literature.

Theorem 2 implies that we can view the proposed conditional density (5) as modeling the noise as a Gaussian random variable followed by marginalizing over \mathbf{M}_n , which is usually achieved by the evidence approximation in the machine learning literature due to the intractability of the integral (Section 3.5 in [35]). Since we have \mathbf{A}, Θ obtained from the previous Sections, we can get the posterior of \mathbf{M}_n from this model:

$$\begin{aligned} p(\mathbf{M}_n | \mathbf{y}_n, \alpha_n, \Theta, \mathbf{D}) &\propto p(\mathbf{y}_n, \mathbf{M}_n | \alpha_n, \Theta, \mathbf{D}) \\ &= p(\mathbf{y}_n | \alpha_n, \mathbf{M}_n, \mathbf{D}) p(\mathbf{M}_n | \Theta) \end{aligned} \quad (35)$$

using the assumption that $p(\mathbf{y}_n)$ is uniform. Maximizing $\log p(\mathbf{M}_n | \mathbf{y}_n, \alpha_n, \Theta, \mathbf{D})$ gives us another minimization problem

$$\begin{aligned} \mathcal{E}(\mathbf{M}_n) &= \frac{1}{2} (\mathbf{y}_n - \mathbf{M}_n^T \alpha_n)^T \mathbf{D}^{-1} (\mathbf{y}_n - \mathbf{M}_n^T \alpha_n) \\ &\quad - \sum_{j=1}^M \log \sum_{k=1}^{K_j} \pi_{jk} \mathcal{N}(\mathbf{m}_{nj} | \boldsymbol{\mu}_{jk}, \boldsymbol{\Sigma}_{jk}) \end{aligned} \quad (36)$$

obtained by plugging (13) and (14) into (35). Note that this objective function has an intuitive interpretation as the first term minimizes the reconstruction error while the second term forces the endmembers close to the centers of each GMM. The weight factor between the two terms is the noise. From an algebraic perspective, since there are also logarithms of sums of Gaussian functions in this objective, we can also use the EM algorithm for ease of optimization. In the E step, the soft membership is calculated by

$$\gamma_{nj k} = \frac{\pi_{jk} \mathcal{N}(\mathbf{m}_{nj} | \boldsymbol{\mu}_{jk}, \boldsymbol{\Sigma}_{jk})}{\sum_k \pi_{jk} \mathcal{N}(\mathbf{m}_{nj} | \boldsymbol{\mu}_{jk}, \boldsymbol{\Sigma}_{jk})}, \quad k = 1, \dots, K_j.$$

In the M step, the derivative w.r.t. \mathbf{m}_{nj} is obtained as

$$\frac{\partial \mathcal{E}}{\partial \mathbf{m}_{nj}} = -\mathbf{D}^{-1} (\mathbf{y}_n - \mathbf{M}_n^T \alpha_n) \alpha_{nj} + \sum_{k=1}^{K_j} \gamma_{nj k} \boldsymbol{\Sigma}_{jk}^{-1} (\mathbf{m}_{nj} - \boldsymbol{\mu}_{jk}).$$

Instead of deploying gradient descent in the M step for estimating the abundances, combining the derivatives for all j actually leads to a closed form solution

$$\begin{aligned} \text{vec}(\mathbf{M}_n^T) &= \left\{ \alpha_n \alpha_n^T \otimes \mathbf{D}^{-1} + \text{diag}(\mathbf{C}_{n1}, \dots, \mathbf{C}_{nM}) \right\}^{-1} \\ &\quad \left\{ \text{vec}(\mathbf{D}^{-1} \mathbf{y}_n \alpha_n^T) + \mathbf{d}_n \right\} \end{aligned}$$

where $\mathbf{C}_{nj} \in \mathbb{R}^{B \times B}$ and $\mathbf{d}_n := (\mathbf{d}_{n1}^T, \dots, \mathbf{d}_{nM}^T)^T \in \mathbb{R}^{MB \times 1}$ are defined as

$$\mathbf{C}_{nj} := \sum_{k=1}^{K_j} \gamma_{nj k} \boldsymbol{\Sigma}_{jk}^{-1}, \quad \mathbf{d}_{nj} := \sum_{k=1}^{K_j} \gamma_{nj k} \boldsymbol{\Sigma}_{jk}^{-1} \boldsymbol{\mu}_{jk}.$$

In practice, despite the need to estimate a huge $M \times B \times N$ matrix, the time cost is actually much less than the estimation of abundances because of the closed form update equation in the M step.

4 Results

In the following experiments, we implemented the algorithm in MATLAB[®] and compared the proposed GMM with NCM, BCM (spectral version with quadratic programming) [14] on synthetic and real images. NCM is implemented as a supervised algorithm wherein we input the ground truth pure pixels, model them by Gaussian distributions, and obtain the abundance maps by maximizing the log-likelihood. Since BCM is also a supervised unmixing algorithm, ground truth pure pixels are again taken as input and the results are the abundance maps. For GMM and NCM, using the algorithm in Section 3.6 we can obtain the endmembers for each pixel. As mentioned previously, the original image data are projected to a subspace with 10 dimensions to speed up the computation for abundance estimation. All the parameters of GMM (except the structure element size r_{se}) are fixed throughout the experiments as $\beta_1 = 5$, $\beta_2 = 5$.

For comparison of endmember distributions, we calculate the L_2 distance $(\int |f(\mathbf{x}) - g(\mathbf{x})|^2 d\mathbf{x})^{1/2}$ between the fitted distribution and the ground truth one, where the latter is only available for the synthetic dataset. For comparison of abundances, we calculate the mean absolute error $\frac{1}{N} \sum_n |\alpha_{nj}^{GT} - \alpha_{nj}^{est}|$ where α_{nj}^{GT} are the ground truth abundances and α_{nj}^{est} are the estimated values. Since only some pure pixels are identified as ground truth in the real datasets, we calculate $error_j = \frac{1}{|\mathcal{I}|} \sum_{n \in \mathcal{I}} |\alpha_{nj}^{GT} - \alpha_{nj}^{est}|$ given the pure pixel index set \mathcal{I} . For comparison of endmembers, the same error formula and overall schema are used, i.e. for an index set \mathcal{I}_j of pure pixels for the j th endmember (in the real datasets), $error_j = \frac{1}{B|\mathcal{I}_j|} \sum_{n \in \mathcal{I}_j} \|\mathbf{m}_{nj}^{GT} - \mathbf{m}_{nj}^{est}\|_1$.

4.1 Synthetic datasets

The algorithms are tested for two cases of synthetic images. The first one is used to test the supervised case, where ground truth endmembers are used to build the distribution parameters such that the abundances and endmembers for each pixel can be estimated. The images are of size 60×60 with 103 wavelengths and created with two endmembers, meadows and painted metal sheets, whose spectra are drawn randomly from the ground truth of the Pavia University dataset (shown in Fig. 1, meadows have 309 samples, painted metal sheets have 941 samples). The abundances are sampled from a Dirichlet distribution so each pixel has random values. Also, an additive noise sampled from $\mathcal{N}(\mathbf{n}_n | \mathbf{0}, \mathbf{D})$ is added to the mixed spectra, where the noise is assumed to be independent at different wavelengths, i.e. $\mathbf{D} = \text{diag}(\sigma_1^2, \dots, \sigma_B^2)$ while σ_k is again sampled from a uniform distribution $[0, \sigma_Y]$. We tested the algorithms for different σ_Y . The effects of priors are all removed in this case, i.e. $\beta_1 = 0$, $\beta_2 = 0$. Fig. 3 shows the box plots of abundance and endmember errors. We can see that GMM has the lowest errors in general for different noise levels. NCM also has relatively low errors in most cases, but tends to produce large errors occasionally (4 out of 20 runs). BCM has the largest errors overall. For the endmembers, although NCM sometimes has lower errors than GMM, the difference is less than 0.002 hence negligible.

Then we move to another case that aims to test the ability to retrieve the endmember distributions. We created a synthetic image with size 60×60 from 4 ground truth endmembers: limestone, basalt, concrete, asphalt. The spectral range is from $0.4\mu\text{m}$ to $14\mu\text{m}$, re-sampled into 200 values. We assume the endmembers are sampled from GMMs following the example in Section 2.3. The means of the GMMs are from the ASTER spectral library [36] (see Fig. 4(a) for their spectra) with slight constant changes. The covariance matrices are constructed by $a_{jk}^2 \mathbf{I}_B + b_{jk}^2 \mathbf{u}_{jk} \mathbf{u}_{jk}^T$ where \mathbf{u}_{jk} is a unit vector controlling the major variation direction. We assume the 4 materials occupy the 4 quadrants of the square image as pure pixels. Then Gaussian smoothing is applied on each abundance map to make the boundary pixels of each quadrant be mixed by the neighboring mate-

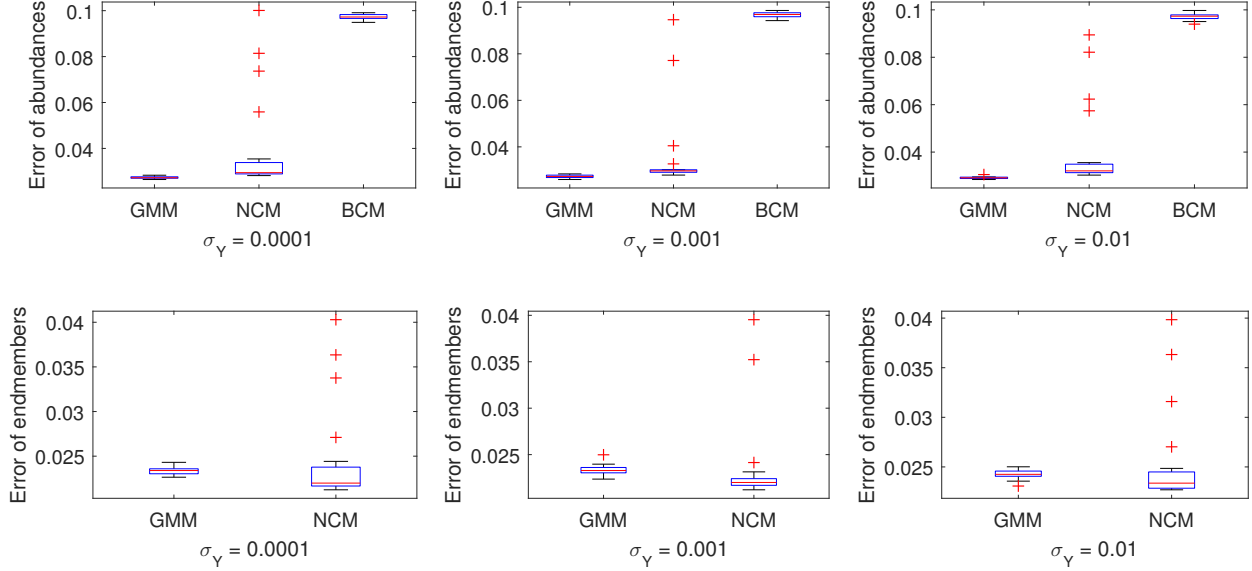


Figure 3: Abundance and endmember error statistics from 20 synthetic images for each noise level in the supervised unmixing scenario.

Table 2: L_2 distance between the fitted distributions (GMM, NCM) and the ground truth distributions for the synthetic dataset.

$\times 10^6$	Limestone	Basalt	Concrete	Asphalt	Mean
GMM	4.16	3.68	3.14	4.27	3.81
NCM	3.94	5.91	4.91	4.07	4.71

rials. Finally, a small amount of noise produced similar to above with $\sigma_Y = 0.001$ is added to the generated pixels. Fig. 4 shows the abundance maps, the original spectra of these materials, and the resulting color image by extracting the bands corresponding to wavelengths 488nm, 556nm, 693nm.

The parameter of GMM was $r_{se} = 5$. Fig. 5 shows the histograms of ground truth pure pixels and the estimated distributions. The ground truth distribution is barely visible as most of the time it coincides with GMM. For limestone and asphalt, all three distributions are similar since the pure pixels are generated by a unimodal Gaussian. However, for basalt and concrete, GMM provides a more accurate estimation while NCM seems inferior due to the single Gaussian assumption. The quantitative analysis in Table 2 implies a similar result by calculating the L_2 distance between the estimated distribution and the ground truth.

Table 3 shows the comparison of abundance errors. The results of BCM and NCM show slightly inferior abundances compared to GMM despite the fact that they have access to pure pixels to train their models.

Table 3: Abundance errors for the synthetic dataset.

$\times 10^{-4}$	Limestone	Basalt	Concrete	Asphalt	Mean
GMM	21	20	21	23	22
NCM	60	42	38	75	54
BCM	62	76	99	157	98

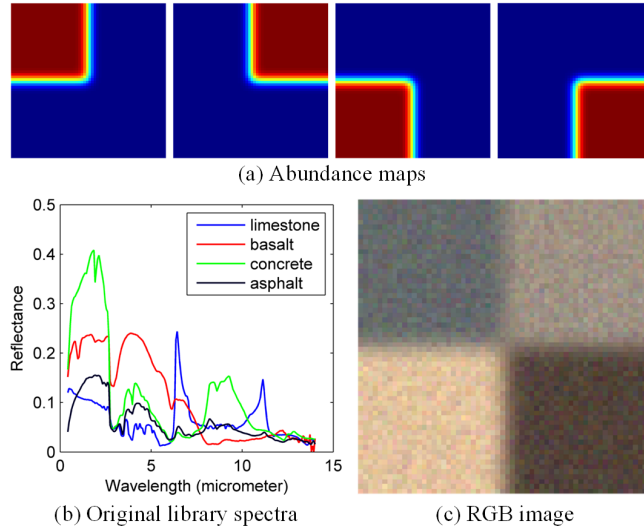


Figure 4: (a) Abundance maps, (b) Original spectra from the ASTER library and (c) Color image of the synthetic dataset.

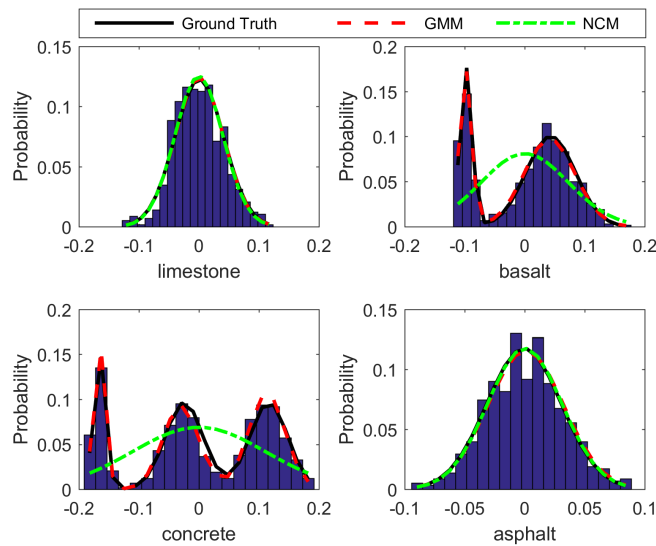


Figure 5: Histograms of pure pixels for the 4 materials (when projected to a 1-dimensional space determined by performing PCA on the pure pixels of each material) and the ground truth and estimated distributions (also projected to the same direction). The probability of each distribution is calculated by multiplying the value of the density function at each bin location with the bin size.

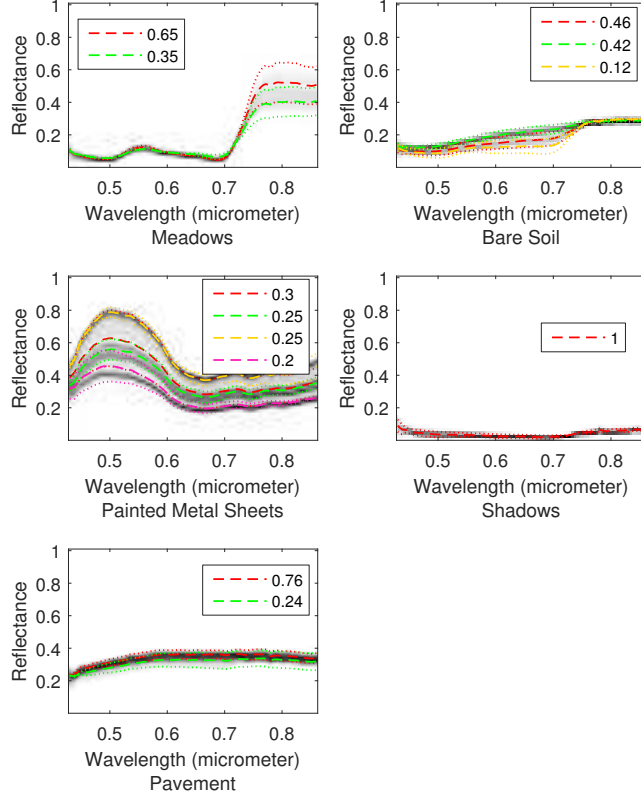


Figure 6: Estimated GMM in the wavelength-reflectance space. The background gray image represents the histogram created by placing the pure pixel spectra into the reflectance bins at each wavelength. The different colors represent different components, where the dashed curve is the center μ_{jk} , the dotted curves are $\mu_{jk} \pm 2\sigma_{jk}\mathbf{v}_{jk}$ (σ_{jk} is the square root of the large eigenvalue of Σ_{jk} while \mathbf{v}_{jk} is the corresponding eigenvector), and the legend shows the prior probability.

4.2 Pavia University

The Pavia University dataset was recorded by the Reflective Optics System Imaging Spectrometer (ROSIS) during a flight over Pavia, northern Italy. The dimension is 340 by 610 with a spatial resolution of 1.3 meters/pixel. It has 103 bands with wavelengths ranging from 430nm to 860nm. As Fig. 1 shows, the original image contains several man-made and natural materials. Considering that the whole dataset contains many different objects, we only performed experiments on the exemplar ROI (47 by 106) shown in Fig. 1, in which 5 endmembers, meadows, bare soil, painted metal sheets, shadows and pavement, are manually identified.

The parameter of GMM is $r_{se} = 2$. Fig. 6 shows the GMM in the wavelength-reflectance space, where we can see the centers and the major variations of the Gaussians. Fig. 7 shows the scatter plot of the results in the projected space. The scatter plot shows that the identified Gaussian components cover the ground truth pure pixels very well. For painted metal sheets, which has a broad range of pure pixels, it estimated 4 components to cover them. For shadows, only one component was estimated. Fig. 8 shows the histograms of pure pixels and the estimated distributions of GMM and NCM. We can see that GMM matches the background histogram better than NCM.

Fig. 9 shows the abundance map comparison. Comparing them with the ground truth shown in Fig. 1(a), we can see that BCM failed to estimate the pure pixels of painted metal sheets, although

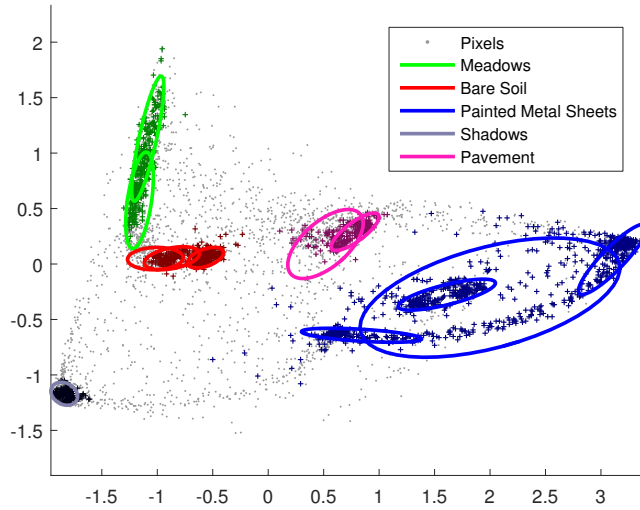


Figure 7: Scatter plot of the Pavia University dataset with the estimated GMM. The gray dots are the projected pixels by PCA. The darkened dots with a color represent the ground truth pure pixels for a material. The ellipses with the same color represent the projected Gaussian components (twice the standard deviation along the major and minor axes, covering 86% of the total probability mass) for one endmember.

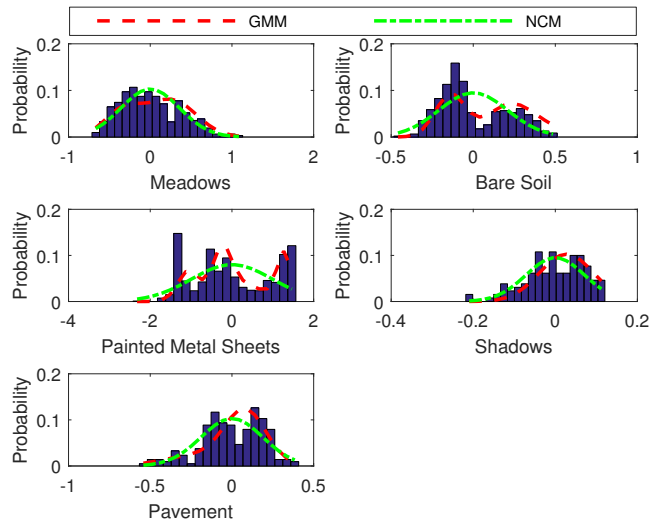


Figure 8: Histograms of pure pixels for the Pavia University dataset and the estimated distributions from GMM and NCM when projected to 1 dimension.

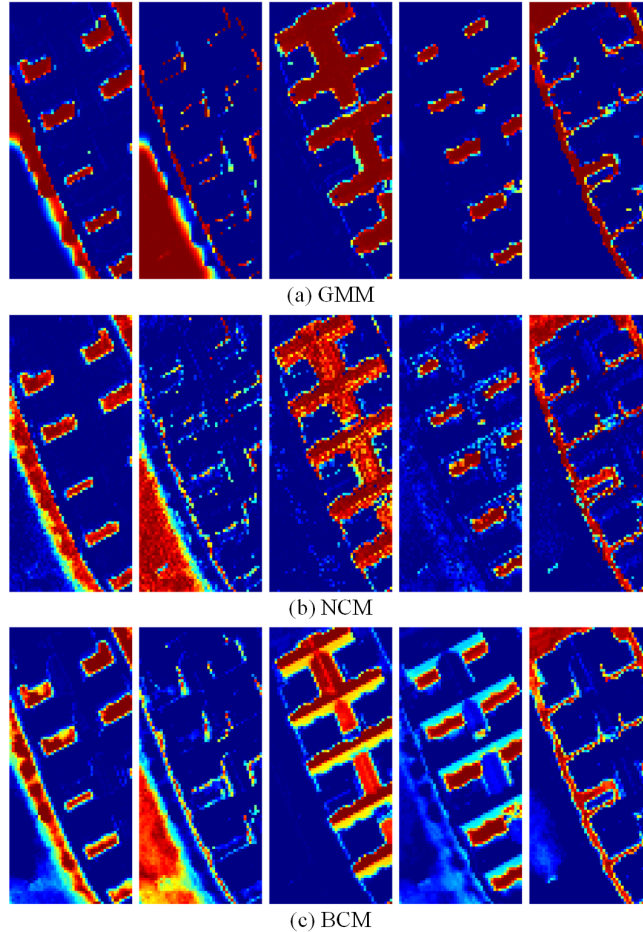


Figure 9: Abundance maps for the Pavia University dataset.

ground truth pure pixels are used for training. For example, the third and fourth abundance maps of BCM show that the pixels in the lower part of painted metal sheets are mixed with shadows, while the reduced reflectances are only caused by angle variation. The result of GMM not only shows sparse abundances for that region, but also interprets the boundary as a combination of neighboring materials. Since this dataset has a spatial spacing of 1.3 meters/pixel, we think this soft transition is more realistic than a simple segmentation. Although the result of NCM looks good in general, the abundances in a pure material region are inconsistent. The errors of abundances and endmembers for these algorithms are shown in Table 4, which implies that GMM performed best overall.

4.3 Mississippi Gulfport

The dataset was collected over the University of Southern Mississippi-Gulfpark Campus [37]. It is a 271 by 284 image with 72 bands corresponding to wavelengths $0.368\mu m$ to $1.043\mu m$. The spatial resolution is 1 meter/pixel. The scene contains several man-made and natural materials including sidewalks, roads, various types of building roofs, concrete, shrubs, trees, and grasses. We selected a 58 by 65 ROI that contains 5 materials. The original RGB image and the selected ROI are shown in Fig. 10(a) while the identified materials and the mean spectra are shown in (b).

Table 4: Abundance and endmember errors for Pavia University.

$\times 1E-4$	Meadow	Soil	Metal	Shadow	Pavement	Mean
GMM	51\35^a	32\23	62\38	12\36	43\31	40\33
NCM	192\93	263\60	488\246	417\41	254\105	323\109
BCM	290	505	602	709	271	475

^a the numbers in ".\" denote the abundance and endmember errors.

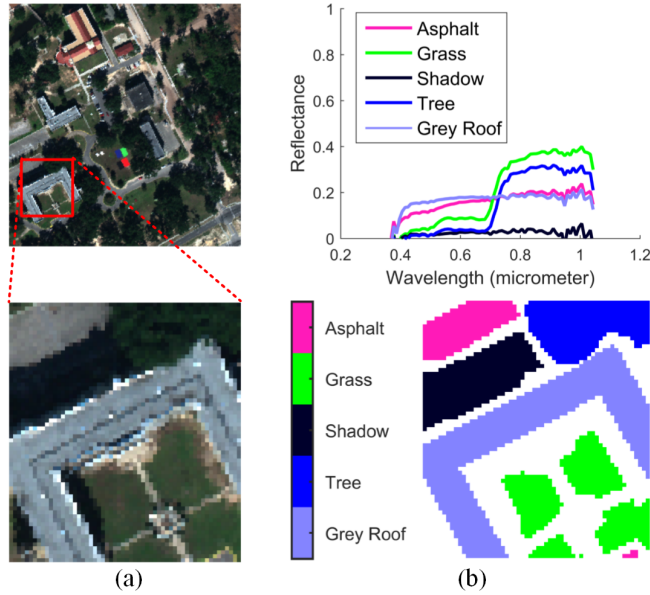


Figure 10: (a) Original RGB image of the Mississippi Gulfport dataset with selected ROI and (b) Ground truth materials in the ROI with their mean spectra.

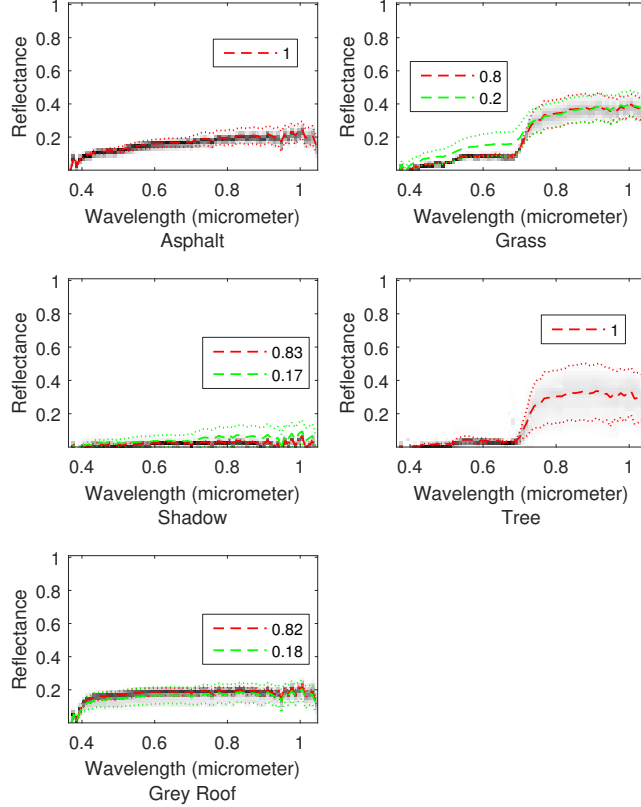


Figure 11: Estimated GMM in the wavelength-reflectance space. The background gray image and the curves have the same meaning as in Fig. 6.

The parameter of GMM is $r_{se} = 1$. Fig. 11 shows the GMM result in the wavelength-reflectance space and Fig. 12 shows the scatter plot. We can see that the estimated Gaussian components successfully cover the identified pure pixels. Fig. 13 shows the estimated distributions. Although there are no multiple peaks in any of the histograms, NCM still does not fit the histograms of shadow and gray roof. In contrast, GMM gives a much better fit for these 2 endmember distributions.

Fig. 14 shows the abundance maps from different algorithms. We can see that GMM matches the ground truth in Fig. 10(b) best, which is also verified in the quantitative analysis in Table 5. Although NCM and BCM take ground truth pure pixels as input, the scattered dots for trees (fourth abundance map) in both of them and the incomplete region of grass for NCM (asphalt for BCM) show their insufficiency in this case.

Table 5: Abundance and endmember errors for the Gulfport dataset.

$\times 1E-4$	Asphalt	Grass	Shadow	Tree	Roof	Mean
GMM	23\54^a	16\39	85\33	217\80	164\73	101\56
NCM	642\76	659\95	577\55	796\192	933\135	722\110
BCM	500	815	568	795	676	671

^a the numbers in ".\" denote the abundance and endmember errors.

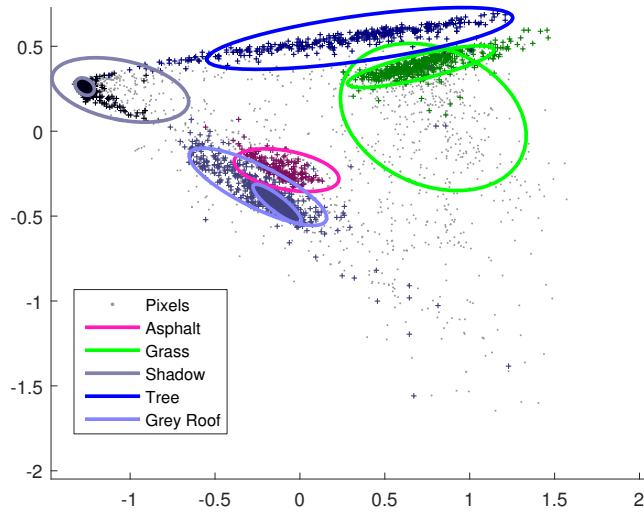


Figure 12: Scatter plot of the Mississippi Gulfport dataset with the estimated GMM. The ellipses and the dots have the same meaning as in Fig. 7.

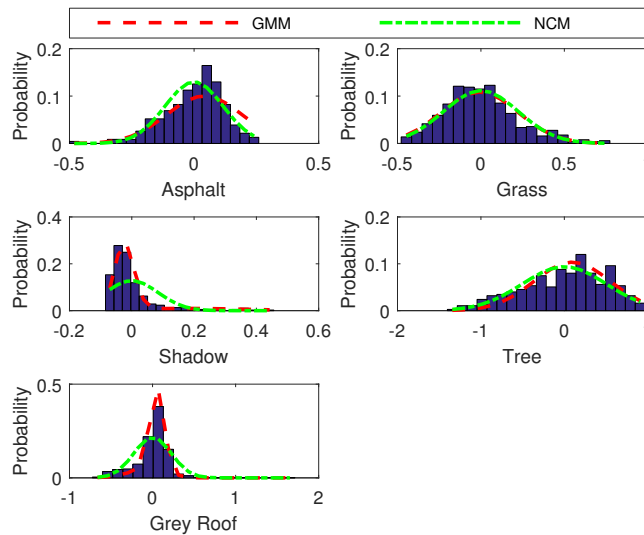


Figure 13: Histograms of pure pixels for the Gulfport dataset and the estimated distributions from GMM and NCM when projected to 1 dimension.

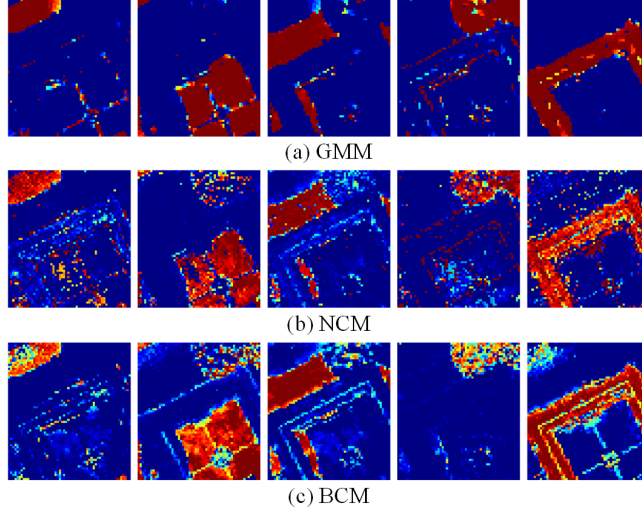


Figure 14: Abundance maps for the Gulfport dataset.

5 Discussion and Conclusion

In this paper, we introduced a GMM approach to represent endmember variability, by observing that the identified pure pixels in real applications usually can not be well fitted by a unimodal distribution as in NCM or BCM. We solved several obstacles in linear unmixing using this distribution, including (i) deriving the conditional probability density function of the mixed pixel given each endmember modeled as GMM from two perspectives; (ii) estimating the abundances and endmember distributions by maximizing the log-likelihood with a prior enforcing abundance smoothness and sparsity; (iii) estimating the endmembers for each pixel given the abundances and distribution parameters. The results on synthetic and real datasets show superior accuracy compared to current popular methods like NCM, BCM. Here we have some final remarks.

Complexity. The abundance estimation algorithm is an iterative process. Since we used projected gradient descent with adaptive step sizes, the number of iterations is usually not large as shown in [38, 30]. For each iteration, it starts with calculating $\boldsymbol{\mu}_{n\mathbf{k}}$ and $\boldsymbol{\Sigma}_{n\mathbf{k}}$ in (6), where storing all $\boldsymbol{\mu}_{n\mathbf{k}}$ ($\boldsymbol{\Sigma}_{n\mathbf{k}}$) requires $O(|\mathcal{K}|NB)$ ($O(|\mathcal{K}|NB^2)$), the computation takes $O(|\mathcal{K}|NMB)$ ($O(|\mathcal{K}|NMB^2)$). Suppose the Cholesky factorization and the matrix inversion of a B by B matrix both take $O(B^3)$ time, and $N \gg B > M$. Evaluating $\log \mathcal{N}(\mathbf{y}_n | \boldsymbol{\mu}_{n\mathbf{k}}, \boldsymbol{\Sigma}_{n\mathbf{k}})$ by the Cholesky factorization will take $O(B^3)$, hence updating all the $\gamma_{n\mathbf{k}}$ takes $O(|\mathcal{K}|NB^3)$, which is also the required time for evaluating the objective function (18). The calculation of $\boldsymbol{\lambda}_{n\mathbf{k}}$, $\boldsymbol{\Psi}_{n\mathbf{k}}$ (in (27) and (28)) will be dominated by the inversion of $\boldsymbol{\Sigma}_{n\mathbf{k}}$ which takes $O(B^3)$, hence the overall calculation takes $O(|\mathcal{K}|NB^3)$ with storage the same as $\boldsymbol{\mu}_{n\mathbf{k}}$ and $\boldsymbol{\Sigma}_{n\mathbf{k}}$. Then if we move to calculating the derivatives in (29), (30) and (31), it is easy to verify that the computational costs are $O(|\mathcal{K}|NMB)$, $O(|\mathcal{K}|NMB^2)$, $O(|\mathcal{K}|NMB^2)$ respectively (Note that \mathbf{K} is a banded matrix so the computation involving it is linear). Reviewing the above process, we conclude that the spatial complexity is dominated by $O(|\mathcal{K}|NB^2)$ and the time complexity is dominated by $O(|\mathcal{K}|NB^3)$. For comparison, the implemented NCM has the same complexity but with $|\mathcal{K}| = 1$. In real applications, with the algorithm implemented in Matlab, running it on the Pavia University and Mississippi Gulfport ROIs requires about 20 minutes and 2 minutes respectively, on a laptop with i7-4700hq CPU and 8GB memory.

Future work. We intend to incorporate endmember variability into nonlinear unmixing.

6 Appendix

6.1 Proof of Theorem 2

We will prove Theorem 2 in the paper, i.e.

$$\int p(\mathbf{y}_n | \boldsymbol{\alpha}_n, \mathbf{M}_n, \mathbf{D}) p(\mathbf{M}_n | \boldsymbol{\Theta}) d\mathbf{M}_n = \sum_{\mathbf{k} \in \mathcal{K}} \pi_{\mathbf{k}} \mathcal{N}(\mathbf{y}_n | \boldsymbol{\mu}_{n\mathbf{k}}, \boldsymbol{\Sigma}_{n\mathbf{k}}) \quad (37)$$

where

$$p(\mathbf{y}_n | \boldsymbol{\alpha}_n, \mathbf{M}_n, \mathbf{D}) = \mathcal{N}\left(\mathbf{y}_n \mid \sum_{j=1}^M \mathbf{m}_{nj} \alpha_{nj}, \mathbf{D}\right)$$

$$p(\mathbf{M}_n | \boldsymbol{\Theta}) = \prod_{j=1}^M \sum_{k=1}^{K_j} \pi_{jk} \mathcal{N}(\mathbf{m}_{nj} | \boldsymbol{\mu}_{jk}, \boldsymbol{\Sigma}_{jk}).$$

Plug them into the left hand side (LHS), it becomes

$$\begin{aligned} \text{LHS} &= \int \mathcal{N}\left(\mathbf{y}_n \mid \sum_j \mathbf{m}_{nj} \alpha_{nj}, \mathbf{D}\right) \prod_{j=1}^M \sum_{k=1}^{K_j} \pi_{jk} \mathcal{N}(\mathbf{m}_{nj} | \boldsymbol{\mu}_{jk}, \boldsymbol{\Sigma}_{jk}) d\mathbf{M}_n \\ &= \int \mathcal{N}\left(\mathbf{y}_n \mid \sum_j \mathbf{m}_{nj} \alpha_{nj}, \mathbf{D}\right) \sum_{\mathbf{k} \in \mathcal{K}} \pi_{\mathbf{k}} \prod_{j=1}^M \mathcal{N}(\mathbf{m}_{nj} | \boldsymbol{\mu}_{jk_j}, \boldsymbol{\Sigma}_{jk_j}) d\mathbf{M}_n \\ &= \sum_{\mathbf{k} \in \mathcal{K}} \pi_{\mathbf{k}} \int \frac{1}{(2\pi)^{\frac{B}{2}} |\mathbf{D}|^{\frac{1}{2}}} e^{-\frac{1}{2}(\mathbf{y}_n - \mathbf{M}_n^T \boldsymbol{\alpha}_n)^T \mathbf{D}^{-1} (\mathbf{y}_n - \mathbf{M}_n^T \boldsymbol{\alpha}_n)} \\ &\quad \prod_{j=1}^M \frac{1}{(2\pi)^{\frac{B}{2}} |\boldsymbol{\Sigma}_{jk_j}|^{\frac{1}{2}}} e^{-\frac{1}{2}(\mathbf{m}_{nj} - \boldsymbol{\mu}_{jk_j})^T \boldsymbol{\Sigma}_{jk_j}^{-1} (\mathbf{m}_{nj} - \boldsymbol{\mu}_{jk_j})} d\mathbf{M}_n. \end{aligned}$$

The product of M Gaussian components in the integral can be written in terms of \mathbf{M}_n . Move the terms not related to \mathbf{M}_n out of the integral, we have

$$\begin{aligned} \text{LHS} &= \sum_{\mathbf{k} \in \mathcal{K}} \pi_{\mathbf{k}} \frac{1}{(2\pi)^{\frac{B}{2}(M+1)} |\mathbf{D}|^{\frac{1}{2}} \prod_j |\boldsymbol{\Sigma}_{jk_j}|^{\frac{1}{2}}} e^{-\frac{1}{2}[\mathbf{y}_n^T \mathbf{D}^{-1} \mathbf{y}_n + \text{vec}(\mathbf{R}_{\mathbf{k}}^T)^T \mathbf{C}_{\mathbf{k}}^{-1} \text{vec}(\mathbf{R}_{\mathbf{k}}^T)]} \\ &\quad \int e^{-\frac{1}{2}\{\text{vec}(\mathbf{M}_n^T)^T \mathbf{Q}_{n\mathbf{k}}^{-1} \text{vec}(\mathbf{M}_n^T) - 2\mathbf{b}_{n\mathbf{k}}^T \text{vec}(\mathbf{M}_n^T)\}} d\mathbf{M}_n, \end{aligned}$$

where $\mathbf{C}_{\mathbf{k}} \in \mathbb{R}^{MB \times MB}$, $\mathbf{Q}_{n\mathbf{k}} \in \mathbb{R}^{MB \times MB}$, $\mathbf{b}_{n\mathbf{k}} \in \mathbb{R}^{MB}$ are defined by

$$\begin{aligned} \mathbf{C}_{\mathbf{k}} &:= \text{diag}(\boldsymbol{\Sigma}_{1k_1}, \dots, \boldsymbol{\Sigma}_{Mk_M}), \\ \mathbf{Q}_{n\mathbf{k}} &:= (\boldsymbol{\alpha}_n \boldsymbol{\alpha}_n^T \otimes \mathbf{D}^{-1} + \mathbf{C}_{\mathbf{k}}^{-1})^{-1}, \\ \mathbf{b}_{n\mathbf{k}} &:= \boldsymbol{\alpha}_n \otimes \mathbf{D}^{-1} \mathbf{y}_n + \mathbf{C}_{\mathbf{k}}^{-1} \text{vec}(\mathbf{R}_{\mathbf{k}}^T) \end{aligned}$$

Using the Gaussian integral, we can have an analytical form for the integration, which gives

$$\text{LHS} = \sum_{\mathbf{k} \in \mathcal{K}} \pi_{\mathbf{k}} \frac{1}{(2\pi)^{\frac{B}{2}} |\mathbf{D}|^{\frac{1}{2}} \prod_j |\boldsymbol{\Sigma}_{jk_j}|^{\frac{1}{2}} |\mathbf{Q}_{n\mathbf{k}}^{-1}|^{\frac{1}{2}}} e^{-\frac{1}{2}\{\mathbf{y}_n^T \mathbf{D}^{-1} \mathbf{y}_n + \text{vec}(\mathbf{R}_{\mathbf{k}}^T)^T \mathbf{C}_{\mathbf{k}}^{-1} \text{vec}(\mathbf{R}_{\mathbf{k}}^T) - \mathbf{b}_{n\mathbf{k}}^T \mathbf{Q}_{n\mathbf{k}} \mathbf{b}_{n\mathbf{k}}\}}.$$

Note the similarity of this form to the right hand side (RHS) of Eq. (37). We can separate the Gaussian function in the RHS of (37) into several parts and show the equivalence of each correspondence.

First, we will introduce a Lemma that will be repeatedly used throughout this Appendix.

Lemma 3. *If $\mathbf{A} \in \mathbb{R}^{d \times B}$, $\mathbf{B} \in \mathbb{R}^{B \times b}$, then $(\boldsymbol{\alpha}_n^T \otimes \mathbf{A}) \mathbf{C}_k (\boldsymbol{\alpha}_n \otimes \mathbf{B}) = \mathbf{A} (\boldsymbol{\Sigma}_{nk} - \mathbf{D}) \mathbf{B}$.*

Proof. Consider the block diagonal nature of \mathbf{C}_k , the block matrix multiplication gives

$$(\boldsymbol{\alpha}_n^T \otimes \mathbf{A}) \mathbf{C}_k (\boldsymbol{\alpha}_n \otimes \mathbf{B}) = \sum_j \alpha_{nj} \mathbf{A} \boldsymbol{\Sigma}_{jk_j} \alpha_{nj} \mathbf{B} = \mathbf{A} \left(\sum_j \alpha_{nj}^2 \boldsymbol{\Sigma}_{jk_j} \right) \mathbf{B} = \mathbf{A} (\boldsymbol{\Sigma}_{nk} - \mathbf{D}) \mathbf{B}.$$

□

Second, we have the following claim that shows the equivalence of the partition function before the exponential term.

Claim 4. $|\boldsymbol{\Sigma}_{nk}| = |\mathbf{D}| \left(\prod_j |\boldsymbol{\Sigma}_{jk_j}| \right) |\mathbf{Q}_{nk}^{-1}|$

Proof. The RHS of this equation can be written as

$$\begin{aligned} \text{RHS} &= |\mathbf{D}| |\mathbf{C}_k| |\boldsymbol{\alpha}_n \boldsymbol{\alpha}_n^T \otimes \mathbf{D}^{-1} + \mathbf{C}_k^{-1}| \\ &= |\mathbf{D}| \left| \boldsymbol{\Sigma}^{\frac{1}{2}} \mathbf{U}^T \right| \left| \left(\boldsymbol{\alpha}_n \otimes \mathbf{D}^{-\frac{1}{2}} \right) \left(\boldsymbol{\alpha}_n^T \otimes \mathbf{D}^{-\frac{1}{2}} \right) + \mathbf{C}_k^{-1} \right| \left| \mathbf{U} \boldsymbol{\Sigma}^{\frac{1}{2}} \right| \end{aligned}$$

where $\mathbf{U} \in \mathbb{R}^{MB \times MB}$ and $\boldsymbol{\Sigma} \in \mathbb{R}^{MB \times MB}$ come from the eigendecomposition of \mathbf{C}_k such that $\mathbf{C}_k = \mathbf{U} \boldsymbol{\Sigma} \mathbf{U}^T$. Since the determinant of a product of matrices equals the product of each determinant, we have

$$\text{RHS} = |\mathbf{D}| \left| \boldsymbol{\Sigma}^{\frac{1}{2}} \mathbf{U}^T \left(\boldsymbol{\alpha}_n \otimes \mathbf{D}^{-\frac{1}{2}} \right) \left(\boldsymbol{\alpha}_n \otimes \mathbf{D}^{-\frac{1}{2}} \right)^T \mathbf{U} \boldsymbol{\Sigma}^{\frac{1}{2}} + \mathbf{I}_{MB} \right|.$$

By Sylvester's determinant theorem, we have

$$\text{RHS} = |\mathbf{D}| \left| \left(\boldsymbol{\alpha}_n \otimes \mathbf{D}^{-\frac{1}{2}} \right)^T \mathbf{C}_k \left(\boldsymbol{\alpha}_n \otimes \mathbf{D}^{-\frac{1}{2}} \right) + \mathbf{I}_B \right|.$$

Apply Lemma 3, we can prove the claim as

$$\begin{aligned} \text{RHS} &= |\mathbf{D}| \left| \mathbf{D}^{-\frac{1}{2}} (\boldsymbol{\Sigma}_{nk} - \mathbf{D}) \mathbf{D}^{-\frac{1}{2}} + \mathbf{I}_B \right| \\ &= \left| \mathbf{D}^{\frac{1}{2}} \right| \left| \mathbf{D}^{-\frac{1}{2}} \boldsymbol{\Sigma}_{nk} \mathbf{D}^{-\frac{1}{2}} \right| \left| \mathbf{D}^{\frac{1}{2}} \right| \\ &= |\boldsymbol{\Sigma}_{nk}|. \end{aligned}$$

□

Finally, we can show the equivalence for the terms in the exponential function. This is given by the following claim.

Claim 5. $\mathbf{y}_n^T \mathbf{D}^{-1} \mathbf{y}_n + \text{vec}(\mathbf{R}_k^T)^T \mathbf{C}_k^{-1} \text{vec}(\mathbf{R}_k^T) - \mathbf{b}_{nk}^T \mathbf{Q}_{nk} \mathbf{b}_{nk} = (\mathbf{y}_n - \boldsymbol{\mu}_{nk})^T \boldsymbol{\Sigma}_{nk}^{-1} (\mathbf{y}_n - \boldsymbol{\mu}_{nk})$.

Proof. Note that the RHS can be expanded as

$$\begin{aligned} \text{RHS} &= (\mathbf{y}_n - \mathbf{R}_k^T \boldsymbol{\alpha}_n)^T \boldsymbol{\Sigma}_{nk}^{-1} (\mathbf{y}_n - \mathbf{R}_k^T \boldsymbol{\alpha}_n) \\ &= \mathbf{y}_n^T \boldsymbol{\Sigma}_{nk}^{-1} \mathbf{y}_n - 2\boldsymbol{\alpha}_n^T \mathbf{R}_k \boldsymbol{\Sigma}_{nk}^{-1} \mathbf{y}_n + \boldsymbol{\alpha}_n^T \mathbf{R}_k \boldsymbol{\Sigma}_{nk}^{-1} \mathbf{R}_k^T \boldsymbol{\alpha}_n, \end{aligned} \quad (38)$$

while \mathbf{Q}_{nk} can be expanded by the Woodbury identity and Lemma 3 as

$$\begin{aligned} \mathbf{Q}_{nk} &= (\boldsymbol{\alpha}_n \boldsymbol{\alpha}_n^T \otimes \mathbf{D}^{-1} + \mathbf{C}_k^{-1})^{-1} \\ &= \left[\left(\boldsymbol{\alpha}_n \otimes \mathbf{D}^{-\frac{1}{2}} \right) \left(\boldsymbol{\alpha}_n \otimes \mathbf{D}^{-\frac{1}{2}} \right)^T + \mathbf{C}_k^{-1} \right]^{-1} \\ &= \mathbf{C}_k - \mathbf{C}_k \left(\boldsymbol{\alpha}_n \otimes \mathbf{D}^{-\frac{1}{2}} \right) \left[\mathbf{I}_B + \left(\boldsymbol{\alpha}_n \otimes \mathbf{D}^{-\frac{1}{2}} \right)^T \mathbf{C}_k \left(\boldsymbol{\alpha}_n \otimes \mathbf{D}^{-\frac{1}{2}} \right) \right]^{-1} \left(\boldsymbol{\alpha}_n \otimes \mathbf{D}^{-\frac{1}{2}} \right)^T \mathbf{C}_k \\ &= \mathbf{C}_k - \mathbf{C}_k (\boldsymbol{\alpha}_n \otimes \mathbf{I}_B) \boldsymbol{\Sigma}_{nk}^{-1} (\boldsymbol{\alpha}_n \otimes \mathbf{I}_B)^T \mathbf{C}_k. \end{aligned} \quad (39)$$

Using the definition of \mathbf{b}_{nk} , the last term in the LHS can be expanded as

$$\begin{aligned} \mathbf{b}_{nk}^T \mathbf{Q}_{nk} \mathbf{b}_{nk} &= (\boldsymbol{\alpha}_n^T \otimes \mathbf{y}_n^T \mathbf{D}^{-1}) \mathbf{Q}_{nk} (\boldsymbol{\alpha}_n \otimes \mathbf{D}^{-1} \mathbf{y}_n) + 2\text{vec}(\mathbf{R}_k^T)^T \mathbf{C}_k^{-1} \mathbf{Q}_{nk} (\boldsymbol{\alpha}_n \otimes \mathbf{D}^{-1} \mathbf{y}_n) \\ &\quad + \text{vec}(\mathbf{R}_k^T)^T \mathbf{C}_k^{-1} \mathbf{Q}_{nk} \mathbf{C}_k^{-1} \text{vec}(\mathbf{R}_k^T). \end{aligned} \quad (40)$$

Plug (38) and (40) into the equality, it can be proved by the following 3 claims. \square

Claim 6. $(\boldsymbol{\alpha}_n^T \otimes \mathbf{y}_n^T \mathbf{D}^{-1}) \mathbf{Q}_{nk} (\boldsymbol{\alpha}_n \otimes \mathbf{D}^{-1} \mathbf{y}_n) = \mathbf{y}_n^T \mathbf{D}^{-1} \mathbf{y}_n - \mathbf{y}_n^T \boldsymbol{\Sigma}_{nk}^{-1} \mathbf{y}_n$

Proof. Plugging the expanded \mathbf{Q}_{nk} in (39) and using Lemma 3 thrice, the LHS can be organized as

$$\begin{aligned} \text{LHS} &= \mathbf{y}_n^T \mathbf{D}^{-1} (\boldsymbol{\Sigma}_{nk} - \mathbf{D}) \mathbf{D}^{-1} \mathbf{y}_n - \mathbf{y}_n^T \mathbf{D}^{-1} (\boldsymbol{\Sigma}_{nk} - \mathbf{D}) \boldsymbol{\Sigma}_{nk}^{-1} (\boldsymbol{\Sigma}_{nk} - \mathbf{D}) \mathbf{D}^{-1} \mathbf{y}_n \\ &= \mathbf{y}_n^T \mathbf{D}^{-1} (\boldsymbol{\Sigma}_{nk} - \mathbf{D}) \mathbf{D}^{-1} \mathbf{y}_n - \mathbf{y}_n^T \mathbf{D}^{-1} (\boldsymbol{\Sigma}_{nk} - 2\mathbf{D} + \mathbf{D} \boldsymbol{\Sigma}_{nk}^{-1} \mathbf{D}) \mathbf{D}^{-1} \mathbf{y}_n \\ &= -\mathbf{y}_n^T \mathbf{D}^{-1} \mathbf{y}_n + 2\mathbf{y}_n^T \mathbf{D}^{-1} \mathbf{y}_n - \mathbf{y}_n^T \boldsymbol{\Sigma}_{nk}^{-1} \mathbf{y}_n \\ &= \mathbf{y}_n^T \mathbf{D}^{-1} \mathbf{y}_n - \mathbf{y}_n^T \boldsymbol{\Sigma}_{nk}^{-1} \mathbf{y}_n. \end{aligned}$$

\square

Claim 7. $\text{vec}(\mathbf{R}_k^T)^T \mathbf{C}_k^{-1} \mathbf{Q}_{nk} (\boldsymbol{\alpha}_n \otimes \mathbf{D}^{-1} \mathbf{y}_n) = \boldsymbol{\alpha}_n^T \mathbf{R}_k \boldsymbol{\Sigma}_{nk}^{-1} \mathbf{y}_n$.

Proof. Again, use the expanded \mathbf{Q}_{nk} and Lemma 3, we have

$$\begin{aligned} \text{LHS} &= \text{vec}(\mathbf{R}_k^T)^T (\boldsymbol{\alpha}_n \otimes \mathbf{D}^{-1} \mathbf{y}_n) - \text{vec}(\mathbf{R}_k^T)^T (\boldsymbol{\alpha}_n \otimes \mathbf{I}_B) \boldsymbol{\Sigma}_{nk}^{-1} (\boldsymbol{\Sigma}_{nk} - \mathbf{D}) \mathbf{D}^{-1} \mathbf{y}_n \\ &= \text{vec}(\mathbf{y}_n^T \mathbf{D}^{-1} \mathbf{R}_k^T \boldsymbol{\alpha}_n)^T - \text{vec}(\mathbf{R}_k^T \boldsymbol{\alpha}_n)^T \boldsymbol{\Sigma}_{nk}^{-1} (\boldsymbol{\Sigma}_{nk} \mathbf{D}^{-1} - \mathbf{I}_B) \mathbf{y}_n \\ &= \boldsymbol{\alpha}_n^T \mathbf{R}_k \mathbf{D}^{-1} \mathbf{y}_n - \boldsymbol{\alpha}_n^T \mathbf{R}_k (\mathbf{D}^{-1} - \boldsymbol{\Sigma}_{nk}^{-1}) \mathbf{y}_n \\ &= \boldsymbol{\alpha}_n^T \mathbf{R}_k \boldsymbol{\Sigma}_{nk}^{-1} \mathbf{y}_n. \end{aligned}$$

\square

Claim 8. $\text{vec}(\mathbf{R}_k^T)^T \mathbf{C}_k^{-1} \text{vec}(\mathbf{R}_k^T) - \text{vec}(\mathbf{R}_k^T)^T \mathbf{C}_k^{-1} \mathbf{Q}_{nk} \mathbf{C}_k^{-1} \text{vec}(\mathbf{R}_k^T) = \boldsymbol{\alpha}_n^T \mathbf{R}_k \boldsymbol{\Sigma}_{nk}^{-1} \mathbf{R}_k^T \boldsymbol{\alpha}_n$

Proof. Finally, simply plugging the expanded \mathbf{Q}_{nk} will prove this last claim

$$\begin{aligned} \text{LHS} &= \text{vec}(\mathbf{R}_{\mathbf{k}}^T)^T (\boldsymbol{\alpha}_n \otimes \mathbf{I}_B) \boldsymbol{\Sigma}_{nk}^{-1} (\boldsymbol{\alpha}_n \otimes \mathbf{I}_B)^T \text{vec}(\mathbf{R}_{\mathbf{k}}^T) \\ &= \text{vec}(\mathbf{R}_{\mathbf{k}}^T \boldsymbol{\alpha}_n)^T \boldsymbol{\Sigma}_{nk}^{-1} \text{vec}(\mathbf{R}_{\mathbf{k}}^T \boldsymbol{\alpha}_n) \\ &= \boldsymbol{\alpha}_n^T \mathbf{R}_{\mathbf{k}} \boldsymbol{\Sigma}_{nk}^{-1} \mathbf{R}_{\mathbf{k}}^T \boldsymbol{\alpha}_n. \end{aligned}$$

□

References

- [1] M. Berman, H. Kiiveri, R. Lagerstrom, A. Ernst, R. Dunne, and J. F. Huntington, “ICE: A statistical approach to identifying endmembers in hyperspectral images,” *IEEE Trans. on Geoscience and Remote Sensing*, vol. 42, no. 10, pp. 2085–2095, 2004.
- [2] J. M. Nascimento and J. M. Bioucas Dias, “Vertex component analysis: A fast algorithm to unmix hyperspectral data,” *IEEE Trans. on Geoscience and Remote Sensing*, vol. 43, no. 4, pp. 898–910, 2005.
- [3] A. Zare, P. D. Gader, O. Bchir, and H. Frigui, “Piecewise convex multiple-model endmember detection and spectral unmixing,” *IEEE Trans. on Geoscience and Remote Sensing*, vol. 51, no. 5, pp. 2853–2862, 2013.
- [4] J. M. Bioucas-Dias, A. Plaza, N. Dobigeon, M. Parente, Q. Du, P. D. Gader, and J. Chanussot, “Hyperspectral unmixing overview: Geometrical, statistical, and sparse regression-based approaches,” *IEEE Journal of Selected Topics in Applied Earth Observations and Remote Sensing*, vol. 5, no. 2, pp. 354–379, 2012.
- [5] N. Keshava and J. F. Mustard, “Spectral unmixing,” *IEEE Signal Processing Magazine*, vol. 19, no. 1, pp. 44–57, 2002.
- [6] B. Hapke, “Bidirectional reflectance spectroscopy: 1. theory,” *Journal of Geophysical Research: Solid Earth (1978–2012)*, vol. 86, no. B4, pp. 3039–3054, 1981.
- [7] A. Halimi, Y. Altmann, N. Dobigeon, and J.-Y. Tournet, “Nonlinear unmixing of hyperspectral images using a generalized bilinear model,” *IEEE Trans. on Geoscience and Remote Sensing*, vol. 49, no. 11, pp. 4153–4162, 2011.
- [8] R. Heylen and P. D. Gader, “Nonlinear spectral unmixing with a linear mixture of intimate mixtures model,” *IEEE Geoscience and Remote Sensing Letters*, vol. 11, no. 7, pp. 1195–1199, 2014.
- [9] J. Broadwater and A. Banerjee, “A generalized kernel for areal and intimate mixtures,” in *2nd Workshop on Hyperspectral Image and Signal Processing: Evolution in Remote Sensing (WHISPERS)*. IEEE, 2010, pp. 1–4.
- [10] J. Broadwater, R. Chellappa, A. Banerjee, and P. Burlina, “Kernel fully constrained least squares abundance estimates,” in *IEEE International Geoscience and Remote Sensing Symposium (IGARSS)*. IEEE, 2007, pp. 4041–4044.

- [11] R. Heylen, M. Parente, and P. D. Gader, “A review of nonlinear hyperspectral unmixing methods,” *IEEE Journal of Selected Topics in Applied Earth Observations and Remote Sensing*, vol. 7, no. 6, pp. 1844–1868, 2014.
- [12] B. Somers, G. P. Asner, L. Tits, and P. Coppin, “Endmember variability in spectral mixture analysis: A review,” *Remote Sensing of Environment*, vol. 115, no. 7, pp. 1603–1616, 2011.
- [13] A. Zare and K. Ho, “Endmember variability in hyperspectral analysis: Addressing spectral variability during spectral unmixing,” *IEEE Signal Processing Magazine*, vol. 31, no. 1, pp. 95–104, 2014.
- [14] X. Du, A. Zare, P. D. Gader, and D. Dranishnikov, “Spatial and spectral unmixing using the Beta compositional model,” *IEEE Journal of Selected Topics in Applied Earth Observations and Remote Sensing*, vol. 7, no. 6, pp. 1994–2003, 2014.
- [15] A. Zare and P. D. Gader, “PCE: Piecewise convex endmember detection,” *IEEE Trans. on Geoscience and Remote Sensing*, vol. 48, no. 6, pp. 2620–2632, 2010.
- [16] D. A. Roberts, M. Gardner, R. Church, S. Ustin, G. Scheer, and R. Green, “Mapping chaparral in the Santa Monica Mountains using multiple endmember spectral mixture models,” *Remote Sensing of Environment*, vol. 65, no. 3, pp. 267–279, 1998.
- [17] A. Halimi, N. Dobigeon, and J.-Y. Tourneret, “Unsupervised unmixing of hyperspectral images accounting for endmember variability,” *IEEE Trans. on Image Processing*, vol. 24, no. 12, pp. 4904–4917, 2015.
- [18] B. Zhang, L. Zhuang, L. Gao, W. Luo, Q. Ran, and Q. Du, “PSO-EM: A hyperspectral unmixing algorithm based on normal compositional model,” *IEEE Trans. on Geoscience and Remote Sensing*, vol. 52, no. 12, pp. 7782–7792, 2014.
- [19] O. Eches, N. Dobigeon, C. Mailhes, and J.-Y. Tourneret, “Bayesian estimation of linear mixtures using the normal compositional model: Application to hyperspectral imagery,” *IEEE Trans. on Image Processing*, vol. 19, no. 6, pp. 1403–1413, 2010.
- [20] O. Eches, N. Dobigeon, and J.-Y. Tourneret, “Estimating the number of endmembers in hyperspectral images using the normal compositional model and a hierarchical Bayesian algorithm,” *IEEE Journal of Selected Topics in Signal Processing*, vol. 4, no. 3, pp. 582–591, 2010.
- [21] D. Stein, “Application of the normal compositional model to the analysis of hyperspectral imagery,” in *IEEE Workshop on Advances in Techniques for Analysis of Remotely Sensed Data*, 2003, pp. 44–51.
- [22] C. A. Bateson, G. P. Asner, and C. A. Wessman, “Endmember bundles: A new approach to incorporating endmember variability into spectral mixture analysis,” *IEEE Trans. on Geoscience and Remote Sensing*, vol. 38, no. 2, pp. 1083–1094, 2000.
- [23] E. B. Wetherley, D. A. Roberts, and J. P. McFadden, “Mapping spectrally similar urban materials at sub-pixel scales,” *Remote Sensing of Environment*, vol. 195, pp. 170–183, 2017.
- [24] J. B. Lee, A. S. Woodyatt, and M. Berman, “Enhancement of high spectral resolution remote-sensing data by a noise-adjusted principal components transform,” *IEEE Transactions on Geoscience and Remote Sensing*, vol. 28, no. 3, pp. 295–304, 1990.

- [25] Y. Zhou, A. Rangarajan, and P. D. Gader, “A spatial compositional model for linear unmixing and endmember uncertainty estimation,” *IEEE Trans. on Image Processing*, vol. 25, no. 12, pp. 5987–6002, 2016.
- [26] D. Achlioptas and F. McSherry, “On spectral learning of mixtures of distributions,” in *Learning Theory*, pp. 458–469. Springer, 2005.
- [27] N. Vlassis and A. Likas, “A greedy EM algorithm for gaussian mixture learning,” *Neural Processing Letters*, vol. 15, no. 1, pp. 77–87, 2002.
- [28] X.-L. Meng and D. B. Rubin, “Maximum likelihood estimation via the ECM algorithm: A general framework,” *Biometrika*, vol. 80, no. 2, pp. 267–278, 1993.
- [29] D. P. Bertsekas, *Nonlinear programming*, Athena Scientific, 1999.
- [30] C.-J. Lin, “Projected gradient methods for nonnegative matrix factorization,” *Neural Computation*, vol. 19, no. 10, pp. 2756–2779, 2007.
- [31] G. J. McLachlan and S. Rathnayake, “On the number of components in a Gaussian mixture model,” *Wiley Interdisciplinary Reviews: Data Mining and Knowledge Discovery*, vol. 4, no. 5, pp. 341–355, 2014.
- [32] P. Smyth, “Model selection for probabilistic clustering using cross-validated likelihood,” *Statistics and Computing*, vol. 10, no. 1, pp. 63–72, 2000.
- [33] L. Gao, Q. Du, B. Zhang, W. Yang, and Y. Wu, “A comparative study on linear regression-based noise estimation for hyperspectral imagery,” *IEEE Journal of Selected Topics in Applied Earth Observations and Remote Sensing*, vol. 6, no. 2, pp. 488–498, 2013.
- [34] R. Roger, “Principal components transform with simple, automatic noise adjustment,” *International Journal of Remote Sensing*, vol. 17, no. 14, pp. 2719–2727, 1996.
- [35] C. M. Bishop, *Pattern recognition and machine learning*, springer New York, 2006.
- [36] A. Baldridge, S. Hook, C. Grove, and G. Rivera, “The ASTER spectral library version 2.0,” *Remote Sensing of Environment*, vol. 113, no. 4, pp. 711–715, 2009.
- [37] P. Gader, A. Zare, R. Close, J. Aitken, and G. Tuell, “MUUFL Gulfport hyperspectral and LiDAR airborne data set,” Tech. Rep. REP-2013-570, Univ. Florida, Gainesville, FL, USA, 2013.
- [38] N. Guan, D. Tao, Z. Luo, and B. Yuan, “Manifold regularized discriminative nonnegative matrix factorization with fast gradient descent,” *IEEE Trans. on Image Processing*, vol. 20, no. 7, pp. 2030–2048, 2011.